Soft Matter

PAPER

View Article Online
View Journal | View Issue

Cite this: *Soft Matter*, 2025, **21**, 6144

Power-law rheology of adherent cells by local optical stretching and implications for mechanical modelling†

Alexander Janik,* Tobias Neckernuss, Kay-E. Gottschalk and Othmar Marti

Received 5th January 2025,
Accepted 1st July 2025

DOI: 10.1039/d5sm00009b

rsc.li/soft-matter-journal

The lack of quantitative agreement between different techniques and publications has been an open issue in cell rheology for many years. Major differences in experimental design – and thus potential sources of the discrepancy – include the magnitude and lateral length scale of force application. To address these issues, we have developed an optical stretcher capable of extracting viscoelastic parameters from adherent cells while applying very low forces of a few pN and deformations of a few nm in a contact-free manner. This paper outlines the potential and limitations of such a setup. The latter include the necessity of reference measurements with the cells in an index-matched medium. It is to our knowledge the first time that adherent cells have been characterized with an optical stretching setup capable of quantitative mechanical measurements. Furthermore, a meta-analysis is conducted with papers measuring the same cell lines by AFM indentation and evaluating the results with the same power-law model. The apparent stiffness values obtained vary by two orders of magnitude, but turn out to be strongly correlated with contact radius as well as applied mechanical stress. The values from optical stretching obtained at low stress and deformation fit into that picture.

1 Introduction

Mechanical phenotyping of cells can be a useful tool to distinguish between healthy and diseased cells, *e.g.* normal and cancerous cells.[1–4] With fast, microfluidics-based techniques, this enables sorting and treatment possibilities.[5] To optimize mechanical phenotyping, *e.g.* sorting criteria, an understanding of the connection of phenomenologic mechanical behavior and underlying cellular structures and mechanisms is desirable. This has however been challenging as cells exhibit a broad range of relaxation times, which is reflected in a power-law compliance over multiple order of magnitude in frequency.[6] Cellular prestress as well as externally applied stress seems to play a crucial role.[7] The optical stretcher presented in this paper employs weak optical interface forces, which allows to probe cells at an external stress two orders of magnitude lower than *e.g.* AFM indentation.

An optical stretcher to mechanically characterize suspended cells was presented by Guck *et al.* in 2000.[8] This device enabled characterisation of cells passing through a microfluidic channel in a contact free manner, and developed into a valuable tool for mechanical phenotyping.[1,9] A setup for adherent cells was devised by our group.[10] It applied stress with a widened laser beam and recorded compliance curves with beads attached to the membrane. Morisaku *et al.* combined a focused 532 nm laser operated at 60 mW to deform cells locally with an interferometric measurement of the deformation.[11] With a photodiode and heterodyne amplification they were able to measure at high frequencies up to 100 kHz. The setup could however not measure the stiffness, as a calibration procedure to determine the height difference from the photodiode voltage was lacking. Furthermore the detection was not phase sensitive, and cell death was induced to 40% of the measured cells due to the intense visible light. The setup presented here is capable of measuring the complex Young's modulus E^*, and the weak optical interface forces allow to do so at a very low stress of approximately 1 Pa.

This paper contains results from the PhD-Thesis "Optical Stretching of Adherent Cells" by A. Janik.[12]

2 Methods

2.1 Optical force

When light crosses the boundary between two media of different refractive index (RI), it excerts a force at the interface. This is due to the higher absolute momentum of a photon in an optically denser medium, and due to radiation pressure from reflection. The momentum change of a transmitted photon is $p_{ph} = \Delta n \cdot 2\pi\nu\hbar/c$,

Institute for Experimental Physics, University of Ulm, Albert-Einstein-Allee 11, 89081 Ulm, Germany. E-mail: alexander.janik@alumni.uni-ulm.de

† Electronic supplementary information (ESI) available. See DOI: https://doi.org/10.1039/d5sm00009b

with the reduced Planck constant $\hbar$, the frequency ν and the speed of light in vacuum c.

The optical force, as calculated from the momentum difference of a photon times the photon rate at an incident power P, becomes:

$$F_{\mathrm{opt}} = \Delta n \cdot P/c. \tag{1}$$

The force given by eqn (1) is applied to the cell membrane with a Ti:Sa-laser operated at 800 nm. It exhibits an approximately Gaussian beam profile, which determines the stress distribution. This is sketched in Fig. 1A.

Reflected photons also cause a momentum transfer to the cell membrane, which however contributes less than 2% to the force as long as the local tilting angle of the membrane is below 40° (see Table 1). For a surface tilted relative to the incident beam there is also refraction. This happens in a way that the optical force, calculated by eqn (1), is perpendicular to the surface being stretched.[8] Based on the height (Table 3) and estimated width (~30 μm) of the cells measured with this setup, a typical 3T3 (HeLa) cell exhibits an average tilting angle of 11.3° (18.1°). Very similar cell heights were found in ref. 13 (Fig. 4 and ESI† therein), while some cells had a diameter of only 20 μm. Surface roughness from caveolae, microvilli and membrane ridges does not give a significant contribution, while surface roughness also seems to be a minor factor (discussion in ESI,† Section S2.1). An average tilting angle of 20° causes an error in the calculated upward force by 6% (Table 1). On a tilted face of the cell, this might be in part compensated by the lateral fraction of the force ($F_{\mathrm{lat}}/F_{\perp}$ = 0.17 at $\alpha_{\mathrm{tilt}} = 10°$) that pulls material towards the measurement spot, so we can neglect this deviation for our cells. For compact or rounded adherent cells, 40° might be exceeded in some areas, so measurements should be acquired *e.g.* above the nucleus.

Lateral gradient forces on dielectric particles inside the cell are also present, but since the laser is much less focused ($1/e^2$ radius w_0 = 1.61 μm) than for a typical optical trap, we do not expect a significant impact on the measurement results. An extended discussion can be found in ESI,† Section S2.2.

2.2 Viscoelastic model for adherent cells

A widespread way to model the viscoelastic properties of adherent cells is to treat them as a viscoelastic continuum. This is common especially for evaluating AFM indentation experiments when hysteresis is taken into account.[14]

The optical stretcher exhibits a Gaussian stress profile, for which the deformation of an elastic half-space can be calculated with an appropriate Green's function for the deformation. This expression connecting stress and strain can then be generalized to the viscoelastic case, which enables calculation of the complex elastic modulus E^*.

The normal component of the displacement effected by a point force of unit amplitude is $u_z = \dfrac{1-\nu^2}{\pi E r} = G(r)$[15] (for a derivation see ref. 16, pp. 50–52). This Green's function of the deformation depends on the distance r and Poisson's ratio ν. The deformation profile can be calculated by convolution of the stress profile $\sigma(r)$ with the Green's function:

$$u_z(r) = (G \times \sigma) = \int \frac{1-\nu^2}{\pi |r-r'|} \frac{1}{E} \sigma(r') \mathrm{d}r'. \tag{2}$$

Inserting the Gaussian stress profile $\sigma(r) = F \dfrac{2}{\pi {w_0}^2} \mathrm{e}^{-2(r/w_0)^2}$, and defining $\delta = u_z(0)$ yields:

$$F = \sqrt{\frac{\pi}{2}} w_0 \frac{E}{1-\nu^2} \delta. \tag{3}$$

This is reminiscent of a widely used formula for the (purely elastic) interpretation of AFM force–distance-curves. For indentation by a sphere with radius R and contact radius a (and $a = \sqrt{R\delta}$), it is:[17]

$$F = \frac{4}{3} a \frac{E}{1-\nu^2} \delta. \tag{4}$$

Our setup measures the average deformation over the area of a focused detection laser spot with an $1/e^2$-radius $0.25 \times w_0$. Based on the deformation profile of an elastic half-space, we deduce the center deformation $\delta = 1.03 \times \delta_{\mathrm{measured}}$.

A general viscoelastic solid exhibits a time dependent elastic modulus $E(t)$ and compliance $J(t)$. Past stress has partly relaxed and is taken into account by a hereditary integral,[18] *i.e.* $(1/E)\sigma$ in eqn (2) is replaced by $(J(t) \times \dot{\sigma}(t))$. For $r = 0$, it reads:

$$\delta(t) = \int \frac{1-\nu^2}{\pi r'} \int_{-\infty}^{t} J(t-t') \dot{\sigma}(r', t') \mathrm{d}t' \mathrm{d}r'. \tag{5}$$

Applying a sinusoidal stress $\sigma = \sigma^* \mathrm{e}^{i\omega t}$ results in a deformation $\delta = \delta^* \mathrm{e}^{i\omega t}$ in a linear system. Insertion into eqn (5) yields:

$$\delta^* = \int \frac{1-\nu^2}{\pi r'} \sigma^*(r') \mathrm{d}r' \times i\omega \int_0^{\infty} J(t') \mathrm{e}^{-i\omega t'} \mathrm{d}t'. \tag{6}$$

With the definition $J^* = i\omega \int_0^{\infty} J(t') \mathrm{e}^{-i\omega t'} \mathrm{d}t'$ and $E^* = 1/J^*$ the relation for the viscoelastic half-space retains the same form as in the elastic case:

$$F = \sqrt{\frac{\pi}{2}} w_0 \frac{E^*}{1-\nu^2} \delta^*. \tag{7}$$

While the asterisks denote complex quantities, the modulation phase of the stretching laser is set to zero, so that σ and F are real numbers and δ^* contains the phase lag of the deformation relative to the excitation.

We compared the model of the cell as a viscoelastic half-space to a model describing a cell as a viscoelastic continuum layer of finite thickness.[12] Stretching 3T3 cells at different beam radii gave similar results when evaluated with the viscoelastic half-space model, contrary to the finite thickness layer. For the latter, large beam radii and flat regions in the cell yielded much lower stiffnesses, which demonstrates the limitations of continuum models to describe adherent cells.

We assume here that the membrane, that experiences the force, is firmly attached to the cell body. The stress required to detach it can be estimated from membrane tether pulling experiments, where a bead is attached to the cell membrane and force is applied with optical tweezers. Literature values are

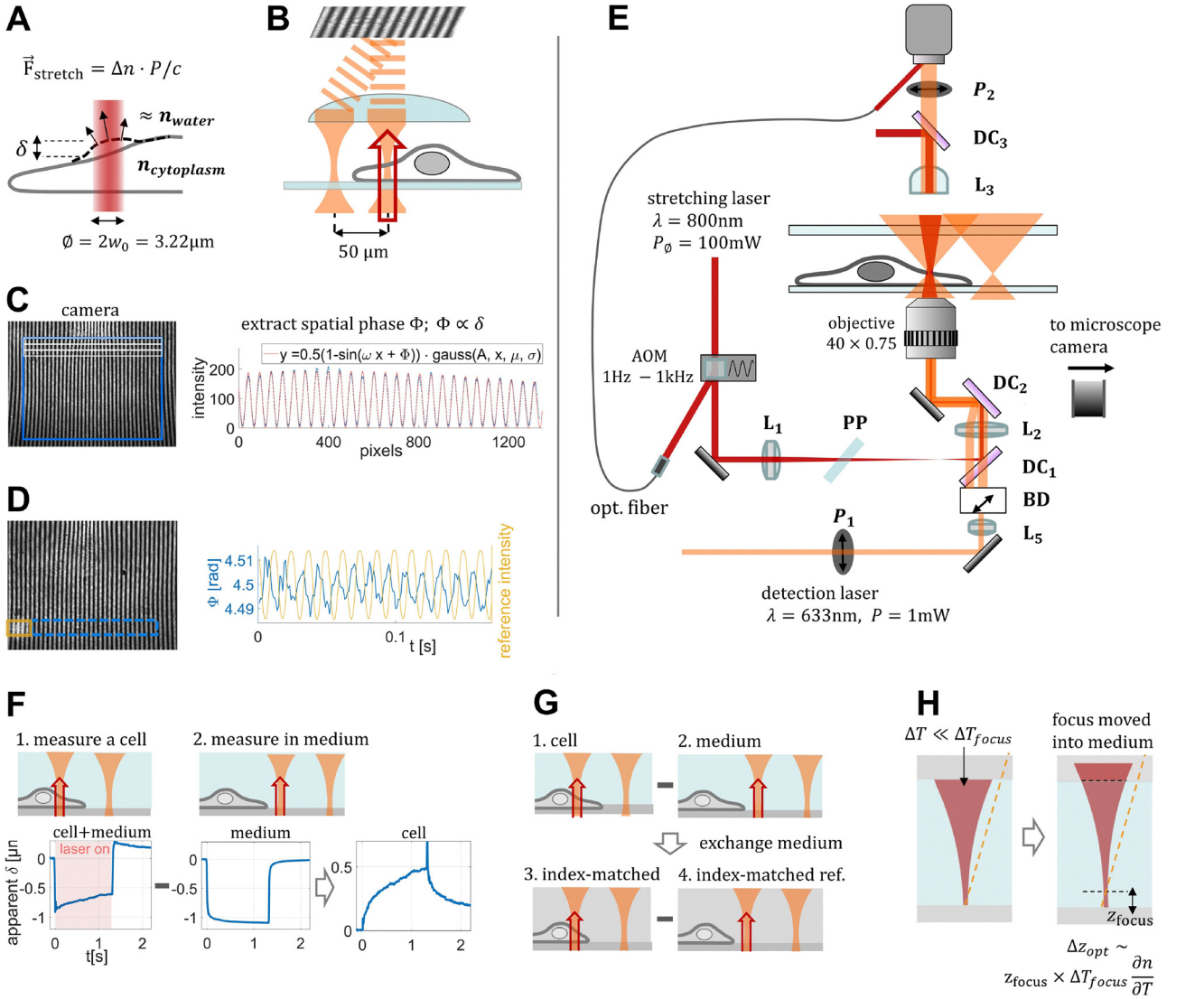

Fig. 1 (A) The stretching laser causes an interface force due to a difference in RI, which acts perpendicular to the cell surface. (B) Beam geometry for creating the interference pattern. The separation distance of the two beams and the focal length of the condenser lens determine the spatial frequency of the stripe pattern. (C) For recording creep curves at up to ~200 fps, most of the camera sensor area can be used. Since the stripes are not perfectly parallel, we split it up vertically into 20 slices, indicated in white, which we fit separately and average the parameters. The deformation δ can then be calculated from the spatial phase Φ *via* eqn (8). (D) For lock-in measurements, the stretching laser intensity is modulated at up to 480 Hz, and a narrow region of interest is chosen to achieve a frame rate of 1000 fps. The reference phase of the stretching laser is extracted from the bright spot, which is created by the optical fiber in (E). (E) Setup for local optical stretching of adherent cells and interferometric detection of the deformation. P: polarizer, BD: beam displacer, DC: dichroid mirror, AOM: acousto-optical modulator for lock-in operation. (F) Recording creep curves of a cytochalasin B treated cell with the laser operated in CW mode (results in Fig. 2). The presence of water in the beam path causes an apparent negative deformation. It is eliminated by performing a reference measurement with the cell moved out of the beam path, and subtracting it. Creep curves reflecting cellular mechanics can only be measured for very soft (treated) cells due to additional intracellular phase shifts caused by the stretching laser (see Fig. 2). (G) For the final technique that we use to characterize untreated cells (Fig. 5), first some cells are measured with lock-in detection. Then the medium is exchanged for an index-matched medium. The same number of cells is subsequently measured to quantify the intracellular non-stretching contributions and subtract them (Section 2.6). The artifact from heating of the water column in lock-in operation is shown in Fig. S6 (ESI†). (H) What remains after the procedure described in F is the optical path length difference from cell deformation plus the difference in absorption between water and index-matched medium within the height of a cell (see eqn (9)). This can be estimated as depicted. The orange dashed line represents the detection angle (12.7°) due to the choice of the blue region on the camera in (D).

listed in Table 2. The stress required to detach membrane is much higher than typical stresses from optical stretching.

2.3 Comparison with AFM indentation

AFM – like optical stretching – applies force mainly perpendicularly to the cell membrane. The force acts upward for optical stretching, but due to the very low stresses it operates in the linear region and should give the same magnitude of deformation as a downward force.

For oscillatory AFM, a cantilever performs small sinusoidal oscillations around an offset indentation. Just as for lock-in optical stretching, it measures $E^*(\omega)$ in the frequency domain,

Table 1 Ratio of the force due to reflected and transmitted photons (F_r/F_t) and ratio of axial force to the total force perpendicular to the membrane for n_{cell} = 1.3674, n_0 = 1.335 (see Section 2.6) and a local tilting angle of the membrane α_{tilt}. F_r/F_t is calculated from the Fresnel equations assuming unpolarized light. For s-polarized light it is about twice that value between 50 and 70. $F_z/F_\perp = \cos\alpha_{tilt}$

α_{tilt}	0°	10°	20°	40°	60°	70°
F_r/F_t	0.012	0.012	0.012	0.019	0.146	1.134
$F_z/F_\perp$	1	0.985	0.94	0.766	0.5	0.342

and very low oscillatory stress and strain can be applied ($<$50 pN and several nanometers for low frequencies in ref. 19) at an almost constant area. Since both δ and a change by a small amount here, the expression deviates from eqn (7) by a prefactor.[20] The total stress is however much higher due to the necessary offset indentation. AFM force–distance curves are measurements in time domain, but give an equivalent result for a linear viscoelastic material.[14]

Typical parameters for the two techniques are compared in Table 2. Force, indentation depth and stress are typically two orders of magnitude higher for AFM. Deeper indentation suggests that structures deeper within the cytoplasma are probed, and a higher force might give different results due to nonlinearities in the material. The latter effect is examined below (Fig. 6). The former seems to be not a dominant factor when comparing the stiffness obtained from different experiments. The stiffness variation turns out to be more so correlated with the lateral dimension of the applied stress (Fig. 6).

This can be rationalized by considering that this width also determines the depth of the 3D stress distribution, and therefore which cellular structures are probed. This is illustrated well by the example of an elastic layer on a stiff underlying substrate of height h, that is indented by a cylindrical probe with radius a. The contribution of the stiff substrate depends on the ratio a/h and not on δ in the linear region.[21] So optical stretching does not probe only the topmost nanometers. It might instead probe a volume comparable to the volume probed by AFM for similar widths of the stress profiles, notwithstanding the much higher deformation for AFM in this case. However, since a living cell is not necessarily linear for AFM and not a continuum, the indentation depth will also affect which structures are probed.

To quantify the width of the stress distribution, we consider eqn (3) and (4). The ratio of the deformations of both techniques at a given total force is $\delta_{opt}/\delta_{sphere} \approx 1.064a/w_0$ for an elastic half-space. If the beam waist equals the size of the contact radius $a = w_0$, the two techniques give virtually the same deformation, so a and w_0 can serve as a lateral dimension of the stress profile. The actual force from optical stretching is much lower, however due to linearity this does not affect the width of the stress distribution. When we compare optical stretching and AFM in Section 5, we estimate a from F and δ with the Hertz formula (eqn (4)), assuming elasticity. We consider this a good estimate, since cells show a more solid-like behavior at low frequencies (Fig. 5: $\beta \sim 0.3$, $E''/E' \sim 0.5$).

2.4 Setup for optical stretching

The setup is depicted in Fig. 1E. Stretching and detection laser are coupled into a custom-built inverted microscope. An objective without immersion (Plan-Neofluar 40 × 0.75, Zeiss, Germany) is used to prevent artifacts from heating of the immersion medium by the stretching laser.

The interferometric detection of the deformation is implemented in an off-axis geometry. The detection laser beam (He–Ne laser P-610, Polytec, Germany; P = 1 mW) is split into two parallel beams by a calcite beam displacer (Melles Griot, 2.7 mm displacement) and focused in the sample plane. This produces two beam waists of $w_0 \approx 0.64$ μm diameter, separated by 50 μm, of which one is centered on the stretched spot on the cell membrane (Fig. 1B). These beams are superimposed by a condenser lens and produce an interference pattern on the camera (BFS-U3-27S5M-C, FLIR, USA). The stretching beam provided by a Ti:Sa laser (Mira-900, Coherent, USA) is focused to w_0 = 1.61 μm on the cell membrane (Fig. 1A), and coupled out by a dichroic mirror. The camera records the interference pattern (Fig. 1C), which is divided into horizontal slices, of which each is fitted by a sinusoidal function with a Gaussian envelope. The average value of the slices yields the spatial phase Φ. Changes in optical path length difference are related to the spatial phase by $\Delta z_{opt}/\lambda_0 = \Delta\Phi/(2\pi)$. With Δn being the difference in RI of the cells and the surrounding medium, the deformation of the membrane can be deduced:

$$\delta = \frac{\Delta\Phi}{2\pi\Delta n}\lambda_0. \quad (8)$$

The median RI of the measured cells was determined as follows. Prior to stretching measurements, the optical path difference of the cell at the measured spot was measured for all cells in regular medium – to estimate the height – and for

Table 2 Typical values for maximum force, lateral dimension, deformation and resulting stress for optical stretching at different input powers and AFM with spherical tips. Parameter ranges for the latter are taken from Tables 6 and 7 and Fig. 6. Stress is calculated by the maximum force divided by the area πw_0^2 and πa^2. The pulling force and stress required to detach membrane from cells has been measured in tether pulling experiments with optical traps. We calculated the stress for ref. 22 by assuming the same bead contact angle as measured in ref. 23. Most measurements for this paper have been conducted either with 1.5 W CW or modulated with P_{mean} = 63 mW. Also w_0 = 1.61 μm was mostly used as the spot is small enough to exhibit high stress/minor stiff substrate effect ($w_0/h \sim 0.5$), and big enough for an almost uniform deformation on the area probed by the detection laser (w_0 = 0.64 μm)

	F_{max} [nN]	a or w_0 [μm]	δ [μm]	σ_{max} [kPa]
AFM	0.5–7	a = 0.4–2.3	0.2–1.5	0.04–110
Opt. stretcher P_{mean} = 63 mW	0.014	w_0 = 1.61	0.01	0.0017
Opt. stretcher P = 1.5 W	0.16	w_0 = 1.61	0.15	0.0201
Membrane detachment	0.035–0.3[22–24]			0.3–0.33 (3T3)[22,23]

Table 3 Median cell height and RI with 25th and 75th percentile for the cells in Fig. 5 above the nucleus and the perinuclear cytoplasm. It is determined by measuring the phase shift for a normal (n_0 = 1.335) and index matched medium (n = 1.3674 ± 0.0005,[26] $\Delta n = n - n_0$ = 0.0324, see Section 2.7

	3T3 cyt	3T3 nucl	HeLa cyt	HeLa nucl
h [μm]	$2.16^{+0.34}_{-0.35}$	$3.10^{+0.59}_{-0.37}$	$3.5^{+1.3}_{-1.0}$	$4.91^{+0.90}_{-0.27}$
Δn	$0.0327^{+0.0032}_{-0.0033}$	$0.0333^{+0.0038}_{-0.0010}$	$0.0338^{+0.0017}_{-0.0011}$	—

most cells later in index matched medium. The results are compiled in Table 3. The RI distribution appears somewhat broadened since it is calculated based on the path length distribution and the assumption of the same, median height. 62% of the measured cells and intracellular locations exhibit an RI within ±10% of Δn = 0.0324. This value is assumed for all cells to calculate the force according to eqn (8). We do not expect the RI variability to significantly broaden the measured stiffness distribution for individual cells. Organelles around the nucleus cause most of the variability in the projected RI (see for instance RI tomograms of HeLa cells in ref. 25). In our measurements, we also see a much higher variability in the perinuclear cytoplasm than above the nucleus, where we avoided to measure above the nucleoli. Most of the organelles however do not exhibit extended areas in contact with the cell membrane and thus do not increase the applied force by the laser. An extended discussion can be found in the ESI,† Section S1 and Fig. S1.

We obtained similar values of Δn by comparing confocal fluorescence height profiles and simultaneously acquired phase shift profiles (Fig. S2, ESI† and Section 2.4.1). From this we estimated the RI of six 3T3 cells in the central part of the cell as n = 0.0302 ± 0.0028. We took these measurements at room temperature, where 31.5% Optiprep (18.9% w/v iodixanol, Δn = 0.0301[26]) resulted in good index matching with phase shifts around zero. The two methods thus agree. At $T = 36^\circ$ we had to increase the Optiprep concentration to 34.5% for good index matching.

The setup implements a contact-free method to determine the deformation, which exhibits low noise due to the almost common beam path of the detection laser beams. The alignment procedure is fairly simple as the two interfering beams are automatically superimposed by a lens.

2.4.1 Validation of the interferometric deformation measurement. To test whether the interferometric setup is capable of reliably measuring optical path length differences of the cytoplasm, fluorescence cross-sections of cells were recorded and compared to simultaneously acquired profiles of optical path length. For that purpose, cell membranes were stained with CellMask deep red plasma membrane stain (Thermo Fisher Scientific, USA), and confocal fluorescence cross-sections were obtained by exciting the dye with the 633 nm detection laser. The results are shown in Fig. S2 (ESI†). Fluorescence height profiles and optical path length difference overlap well, also in regions of the cell with a tilted surface.

A curved surface from optical deformation can lead to a lensing effect, which has been exploited for measurements of the optical deformability of liquids.[27] To estimate the impact on our interferometric measurements of the deformation, we measured the diameter of d = 1.57 μm and d = 4.5 μm silica beads in a glycerol/water mixture (S2.3 and Fig. S3A, ESI†). This provides surfaces with a defined curvature, and the RI difference to the medium was adjusted to be similar to cells $\Delta n \sim 0.0324$. We conclude, that due to the lensing effect, our setup underestimates the real deformation by at most 16%.

2.4.2 Lock-in measurements. For dynamic measurements, the laser intensity is modulated sinusoidally by an acousto-optical modulator (DTSXY-400, AA Opto-Electronic, France). A beam from a higher diffraction order is coupled into a fiber (see Fig. 1E), and guided to the edge of the camera sensor. The intensity of this bright spot on the camera is also modulated by the AOM with a phase shift of π relative to the intensity of the stretching laser (Fig. 1D). From the intensity over time, the phase of the stretching laser is retrieved *via* a fast Fourier transform. Subtracting the modulation phase from the measured phase of the deformation allows the calculation of the phase lag and thus the complex Young's modulus.

To measure the phase shift over time, a narrow region of interest is chosen (196 pixels vertically, 48 after 4× vertical binning) near the lower edge of the camera. This enables a frame rate of up to 1 kHz and results in a detection angle of $\sim 12.5^\circ$. A few modulation frequencies between 1 Hz and 500 kHz are chosen and sequentially applied to a cell for 10 s (or 20 s at 1 Hz). A measurement at a single spot thus takes about 60 s. Amplitude and phase lag are determined by a fast Fourier transform and filtering for each frequency, which results in a bandpass filter width of 0.1 Hz (0.05 Hz) at 1000 fps.

2.5 Removal of phase shifts due to heating of the water column

The raw signal obtained from a creep measurement of a NIH-3T3 cell treated with 10 μmol L^{-1} cytochalasin B is plotted in Fig. 1F, left. It is dominated by an apparently negative deformation, which appears as soon as water is present in the beam path. Water exhibits significant absorption in the near infrared, which results in heating, a lower mass density of water, and a decrease in RI by $\frac{\partial n}{\partial T} = 13.2 \times 10^{-5}\ ^\circ\mathrm{C}^{-1}$.[28] Since temperature increases more in the measurement beam than in the reference beam 50 μm away, this results in a shift of the measured relative phase. A mean temperature difference of 1 °C in a chamber of 500 μm height would for example result in an apparent deformation of $\delta = \Delta T \frac{\partial n}{\partial T} z \frac{1}{\Delta n_{\mathrm{cell}}} = 2$ μm.

Therefore an additional reference measurement is acquired with both 633 nm beams off the cell (Fig. 1F). The apparent deformation from heating of the water column is subtracted from the stretching measurement to eliminate the artifact, and finally obtain a creep curve of the cell. In the resulting creep curve in Fig. 1F there is a spike at the time the shutter is closed, which stems from the fact that shutter and camera (100 fps in this measurement, illumination time <5 ms) are not synchronized. Therefore, stretching and reference measurement to be subtracted do not necessarily exhibit the same number of

frames while the shutter is open. A significant fraction of the cell are molecules other than water. However, subtracting the phase shift from water still largely removes this artifact, since most of it is caused by the ≈500 μm water column above the cell. For lock-in measurements, the water contribution for each frequency is subtracted in the same way (Fig. S6, ESI†).

We checked whether the presence of a temperature gradient above the cell could cause a relative change in the measured path length difference. If this was the case, some artifact would still be present after subtracting a reference measurement without a cell. After our measurements of beads in glycerol:water mixtures we can rule out such an effect (Section S2.3 and Fig. S3B, ESI†).

2.5.1 Negligible impact of heating on cellular mechanics. In the suspended cell optical stretcher, a laser with a diameter slightly larger than a suspended cell, operated at 1064 nm, induces heating of 13.3 K W^{-1}. At a power of 1 W, the temperature change was shown to strongly alter cell mechanics.[29] For tightly focused optical tweezers at the common wavelength of 1064 nm, the temperature increase found by different authors was in a range of 1 to 3 °C per 100 mW.[30] The absorption coefficient of water at 800 nm is however lower by a factor of about 6.7.[31] In combination with the low power necessary to stretch adherent cells with this setup (P_{ptp} = 126 mW for the lock-in technique) and a larger beam waist w_0 = 1.61 μm, this leads to negligible heating of ∼0.3 °C.

2.6 Removal of intracellular non-stretching contributions by index matching

In a next step, it was tested whether the setup is capable of differentiating between stiff, untreated adherent cells, and cells that were softened with 10 μmol L^{-1} cytochalasin B (Cayman Chemical Company, USA), which disrupts the actin cytoskeleton. Creep curves were recorded with the stretching laser in CW operation at a high power (P ≈ 1.5 W), and are shown in Fig. 2. After subtraction of the reference measurement next to the cell (see Fig. 1F), the deformation is mostly negative for untreated cells, while it looks more like a typical creep curve for treated cells. The setup is clearly able to distinguish between the groups on both timescales with these creep compliance measurements; however, a quantitative characterization of untreated cells was not possible. The stretching laser apparently drives other processes besides stretching, which cause a negative phase shift. To quantify these effects, we established the lock-in technique for higher resolution.

The laser intensity is sinusoidally modulated at a few frequencies, and only a narrow band around the excitation frequency is selected. Fig. 3, left shows the in-phase and out-of-phase deformation of HeLa cells probed above the perinuclear cytoplasm. As already observed in the creep experiments (Fig. 2), high modulation frequencies result in apparently negative deformations. There seem to be interactions between the laser and the cell that leads to an excess negative phase shift compared to water. To test this hypothesis, cells were measured in an index matched medium (n = 1.3674, see Section 2.7). Since the optical force pulling the membrane upwards is proportional to Δn (eqn (10)), index matching eliminates the optical force at the membrane, but keeps the cell interior unaltered.

Fig. 3, middle, shows such a measurement. After removal of the (positive) stretching contribution, the resulting apparent

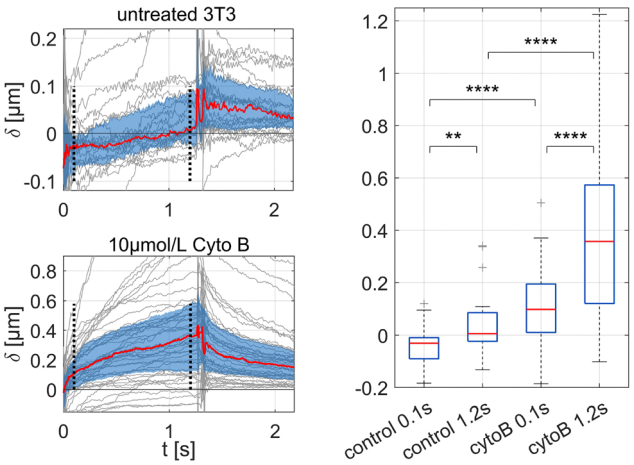

Fig. 2 Left: Creep curves of n = 44 cytochalasin B-treated and n = 25 untreated NIH-3T3 cells. The stretching laser is on from 0 to 1.3 s at P_{sample} ≈ 1.5 W. The blue area shows the inter-quartile range and the red line the median. Right: The boxes are extracted from the creep curves in the left at times indicated by the dashed lines. P-Values ($p < 0.01$ and $p < 0.0001$) were obtained by a Wilcoxon rank sum test. The disturbances around 0 s and 1.3 s stem from a shorter shutter open time of 1.25 s for some measurements, a variability of ±0.005 s, and no synchronisation with the camera.

deformation is negative. This indicates that the stretching laser causes a negative phase shift inside the cell. Plausible explanations are thermophoresis or intracellular absorptive heating that differs from water, as discussed at the end of Section 2.6.

The stretching contribution of the signal in Fig. 3, right, can be obtained by subtracting the median index matched signal from the stretching measurements. After this step, a positive signal remains as expected (Fig. 3, right). From then on, all samples were measured first in the regular medium and subsequently in an index matched medium with a similar osmolarity and concentration of nutrients.

When analyzing the reference measurements mathematically, we can dissect the signal into phase shifts within the lowest microns $\Delta\phi_{0-3\mu m}$ (where the cell is at) and $\Delta\phi_{3-500\mu m}$ (the water column above the cell), into absorption by water ($\Delta\phi_{absWater}$), and index-matched solution ($\Delta\phi_{absIdxmatched}$, about 1.5× as high), into stretching ($\Delta\phi_{stretch}$) and intracellular non-stretching ($\Delta\phi_{intracell}$). Then the signal after subtraction of the reference measurements as depicted in Fig. 1G can be written as

$$\begin{aligned}\Delta\phi &= \left[\Delta\phi_{stretch} + \Delta\phi_{intracell} + \Delta\phi_{absWater,3-500\mu m}\right] \\ &\quad - \left[\Delta\phi_{absWater,0-3\mu m} + \Delta\phi_{absWater,3-500\mu m}\right] \\ &\quad - \left[\Delta\phi_{intracell} + \Delta\phi_{absIdxmatched,3-500\mu m}\right] \\ &\quad + \left[\Delta\phi_{absIdxmatched,0-3\mu m} + \Delta\phi_{absIdxmatched,3-500\mu m}\right] \\ &= \Delta\phi_{stretch} + \Delta\phi_{absIdxmatched,0-3\mu m} - \Delta\phi_{absWater,0-3\mu m}\end{aligned} \quad (9)$$

The first two square brackets correspond to the measurements in regular medium, the latter two in index-matched solution. What remains is stretching plus the negative phase

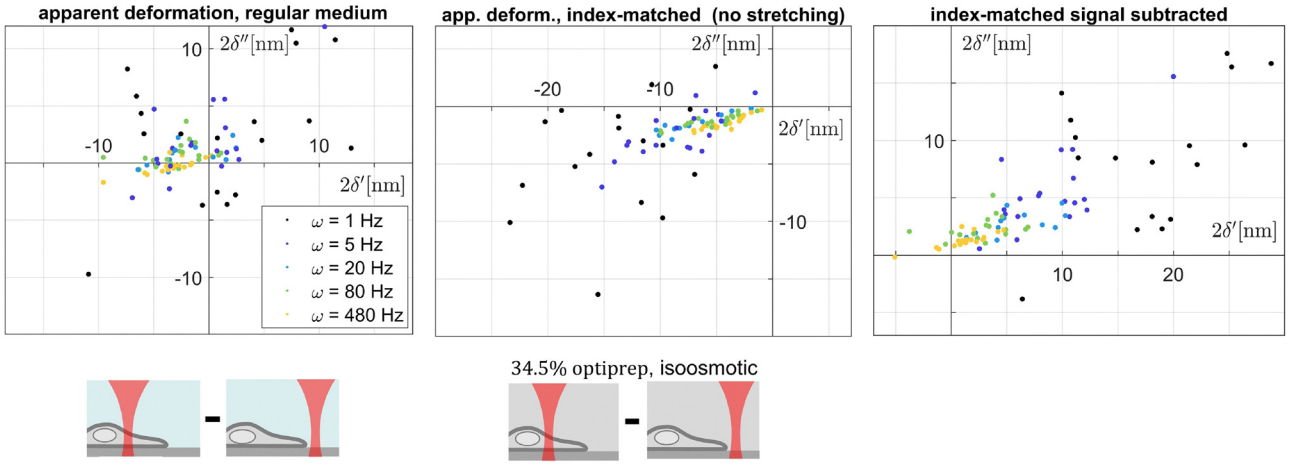

Fig. 3 Apparent peak-to-peak deformation of untreated HeLa cells when measured in culture medium, where 34.5% of the volume is replaced first by sodium chloride solution and subsequently by the density gradient medium Optiprep (Serumwerk Bernburg AG, Germany), to match the RI of the cytoplasm. Small amounts of Dulbecco's modified Eagle medium, DMEM (DMEM) powder and glucose are added to compensate for the lower nutrient concentration. In the diagram on the right, the EHA has been corrected for as described in Section 2.6. The schematics in the bottom also show the reference measurement in medium.

shift within the lowest microns of index-matched medium in excess of water. The index-matched solution absorbs about 1.5× as water, so we term it the excess heating artifact (EHA). We estimate the heating of the lowest microns by measuring how $\Delta\phi$ changes when the stretching laser beam waist is moved from the cover slip top into the medium. This is depicted in Fig. 1H. Since the widened laser beam at the top of the chamber causes much less of a temperature change than in the focus, these measurements approximate $\Delta\phi_{\mathrm{absWater,0–3\mu m}}$ or $\Delta\phi_{\mathrm{absIdxmatched,0–3\mu m}}$. We measured the apparent deformation over focal height for both media and all 5 frequencies (Fig. S7, ESI†). From the fit parameters we calculate a correction factor for each cell depending on the membrane z position during the measurement. Our thermal simulations[12] show that ∼20% of the temperature increase are due to the increased distance of the focus from the borosilicate glass cover slip, which cools the adjacent medium due to its higher heat conductance. Overall, we estimate that the true EHA to subtract is the value obtained by the focal shift measurement, reduced by a factor of ×0.5 to ×0.75. We conservatively assume 0.5× for data evaluation, but additionally calculated the mechanical constants from our experiments with cells for ×0.75 in Table 4. The difference on β is less than 4%, for E_0 it is up to 8%. Given the large discrepancies between different methods in cell rheology we deem that acceptable.

Table 4 The median mechanical parameters E_0 and β for the cells measured by optical stretching (Fig. 4) in dependence of the weighting factor for the measured EHA ($\mathrm{EHA_m}$). Cells were measured above the perinuclear cytoplasm and the nucleus

	3T3		HeLa	
	E_0 [Pa]/β perinucl.	E_0 [Pa]/β nucl.	E_0 [Pa]/β perinucl.	E_0 [Pa]/β nucl.
0.5 × $\mathrm{EHA_m}$	208/0.281	258/0.382	180/0.324	301/0.293
0.75 × $\mathrm{EHA_m}$	198/0.284	248/0.377	166/0.330	279/0.304

2.6.1 Potential explanations of the negative phase shift. One potential explanation is absorptive heating. If it was twice as high inside a cell compared to water, this would result in additional ΔT = 0.3 °C. With $\frac{\partial n}{\partial T} = 13.2 \times 10^{-5}\ \mathrm{K^{-1}}$,[28] and for 5 μm with temperature elevated by ΔT = 0.3 °C, this would result in an apparent deformation of 6.1 nm. This is the correct order of magnitude but somewhat low (Fig. 3, middle). Furthermore, such a significant extra absorptive heating in the near infrared might double the temperature increase in optical traps compared to water, and has to our knowledge not been observed before. Thermophoresis is a phenomenon where particles move down a temperature gradient, which can lead to reduced concentrations in a laser beam. In the stationary state, a concentration ratio $c_{\mathrm{hot}}/c_{\mathrm{cold}} = \exp(-\Delta T \cdot S_{\mathrm{T}})$ forms, with the Soret coefficient S_{T}.[32] For absorptive heating of water (T/P = 3 K W^{-1} at 800 nm, Section 2.5), $\Delta T(126\ \mathrm{mW_{ptp}}) \approx 0.3$ K for optical stretching. S_{T} is on the order of 0.1 K^{-1} for proteins[32] and 0.3 to 0.4 K^{-1} for 50 nm polystyrene particles.[33] Even when conservatively assuming 0.1 K^{-1}, $c_{\mathrm{hot}}/c_{\mathrm{cold}}$ = 0.97. This impacts the optical path length we measure in a similar way as if the cell were compressed by 3%. For a 3 μm cell that corresponds to an apparent negative deformation of 90 nm. Even though the particles cannot move freely in the cytoplasm, this effect could thus be strong enough to explain the apparent negative phase shift. For a 30 μm beam waist, thermophoresis happens on a timescale of seconds to minutes,[32] but it scales with the square of the width of the temperature gradient,[33] which makes it a plausible explanation for the negative phase shift. An observation that also fits into the picture is that increasing the beam waist by a factor of 2 at the same power reduces the negative phase shift by a factor of 2.[12]

2.7 Cell culture and treatment and PDMS thin film preparation

NIH-3T3 mouse fibroblast cells (ATCC CRL-1658, Virginia, USA) and HeLa cells (Sigma Aldrich, Germany) were cultured in

DMEM with 4.5 g L^{-1} glucose (Gibco by life technologies, Germany), 1% antibiotic/antifungal solution (GE Healthcare, USA), and 10% fetal bovine serum (FBS, Bio&Sell, Germany), in a humid atmosphere at 5% CO_2. 20 hours prior to measurement cells were detached with Trypsin (Biowest, France), and about 110 000 cells were allowed to adhere to a fibronectin-coated (fibronectin human plasma, Merck KGaA, Germany) glass cover slip (170 ± 5) μm in a ∅ 60 mm Petri dish.

On the day of the measurement, the cover slip was inserted into a custom built sample chamber of 0.5 mm height, which was filled with DMEM medium (Gibco by life technologies, Germany; same formulation as above but no phenol red, no FBS, 5.958 g L^{-1} HEPES pH buffer). We did not add FBS for the measurements in this paper, since it seemed to add noise to the interferometric signal. However, we later quantified it and found that there is no appreciable extra noise in lock-in measurement mode (see Fig. S6, ESI†), so it can in principle be used. This medium was CO_2-enriched by keeping it in an incubator at 5% CO_2 over night and introduced into the sealed chamber shortly before the measurements started. For the lock-in technique, cells were first measured in a DMEM-solution (65.5% DMEM/HEPES, 34.5% water, 8.2 g L^{-1} NaCl, 2.8 g L^{-1} glucose and 4.8 g L^{-1} DMEM powder, high glucose the latter from Gibco by life technologies, Germany). Subsequently, the same amount of cells were measured in a solution with a RI of $n = 1.3674 \pm 0.0005$ (estimated based on Table 2 in ref. 26). This index matched solution contained 65.5% DMEM/HEPES, 34.5 vol% Optiprep (Serumwerk Bernburg AG, Germany; density gradient medium with the X-ray contrast agent Iodixanol), 2.8 g L^{-1} glucose and 4.8 g L^{-1} DMEM powder. The osmolarity of DMEM- and index matched solution were estimated to be 346.9 mosm L^{-1} and 348.7 mosm L^{-1}, respectively, similar to the cell culture medium (341 mosm L^{-1}).[34] These values were calculated based on particle concentrations. For Optiprep, molecular interactions and resulting lower osmolarity were taken into account based on dilution curves of iodixanol-based X-ray contrast agents.[35]

In Optiprep containing medium, the average phase shift caused by cells in the beam path stayed around zero for at least 2–4 hours at $T = 36$ °C, indicating that no significant amounts of iodixanol molecules enter the cytoplasm. No obvious changes in morphology were induced by the agent over the mentioned time period.

Measurements were carried out at (36 ± 1) °C.

To obtain well-defined reference samples we prepared thin films of Sylgard 184 silicone elastomer (Dow Corning, Wiesbaden, Germany) by spin coating. Different ratios of base to crosslinking agent were mixed for five minutes and degassed in vacuum for 15 minutes. Cover slips were plasma treated to promote adhesion, and spin coated right after at 7000 rpm for 90 seconds. This resulted in an average film thickness of about 10 μm. To examine the impact of the spinning speed, about half of the PDMS films have instead been produced by diluting PDMS in Hexane at a weight ratio of 1 : 5 and spincoating at 250 rpm. Both preparation methods yielded the same viscoelasticity from optical stretching (Fig. S8, ESI†). 3 mm thick bulk samples were created by pouring the elastomer mixture on a glass surface covered with PTFE tape to prevent sticking. All samples were baked in the oven at 100 °C for 90 minutes.

3 Optical stretching rheology of PDMS thin films

For further validation of the optical stretcher we fabricated soft 10 μm PDMS thin films by spin coating as described in Section 2.7. Hydrogels in water mechanically resemble cells more, but are unsuitable for optical stretching due to their low RI difference, *e.g.* $\Delta n = 0.005$ and $E = 4.5$ kPa for poly-acrylamide gel with 3.25% crosslinker.[36] As previously mentioned, the sensitivity of optical stretching at a given power scales with Δn^2. For PDMS in air, $\Delta n = 0.41$ and from Fresnel's formulae follows that $R = \Delta n^2/(1 + n)^2 = 2.89\%$ of the photons are reflected on the interface. The force applied by the laser beam therefore becomes

$$F_{\mathrm{opt}} = [\Delta n(1 - R) + 2R]\cdot P/c = 0.46P/c. \qquad (10)$$

For a given power the force is thus about 15 times higher and the optical path length difference for a given deformation is $\Delta n/\Delta n_{\mathrm{cells}} \gtrsim 10$ times higher than for cells. The sensitivity is therefore about 150 times higher, and at $P = 1$ W_{ptp} we are thus able to measure much stiffer PDMS samples with mixing ratios of 1 : 36 (0.1 MPa) to 1 : 100 (1 kPa). We also include a stiff substrate correction factor $\delta_\infty = 1.125\delta_{\mathrm{measured}}$ to account for the finite thickness of the sample[12] (even higher for spherical tip AFM[37]).

AFM studies of PDMS-films with mixing ratios lower than 1 : 36 are scarce, presumably due to co-occurrence of high viscosity, surface tension and stickiness (work of separation much higher than work of adhesion[38]). In the only study we found the results differ dramatically from bulk measurements for 1 : 60 and 1 : 80 films.[39] We therefore performed reference measurements with a shear rheometer (Kinexus Prime Pro+, Malvern Panalytical, UK) on 3 mm thick bulk samples, which allows to extract only viscoelasticity. The complex bulk modulus for the different mixing ratios is shown in Fig. 4B.

We observed that besides the stretching-induced phase shift, there is also a negative phase shift in the films – a phenomenon that also occurs for cells (Fig. 3). Fig. 4A shows the apparent deformation for stiff 1 : 20 films over the film thickness, presumably caused by a temperature increase and a resulting RI change. Higher crosslinker ratios gave more uneven films and less reproducible negative phase shifts, so we performed reference measurements on 1 : 20 films and subtracted the signal, analogous to the index-matched reference measurements with cells. Since 1 : 20 films are only about 6 times stiffer than 1 : 36 (Fig. 4B) there is also a small deformation that gets erroneously subtracted. We estimate this δ_{err} based on rheometer stiffness, and add $\delta_{\mathrm{err}} \times 1/1.2$ since optical stretching might yield slightly lower deformations (see below). The Malvern rheometer is only calibrated up to 10 Hz so we use the curve from Chen *et al.*[40] for higher frequencies (Fig. 4B, perfect agreement for E', and δ'' is negligible).

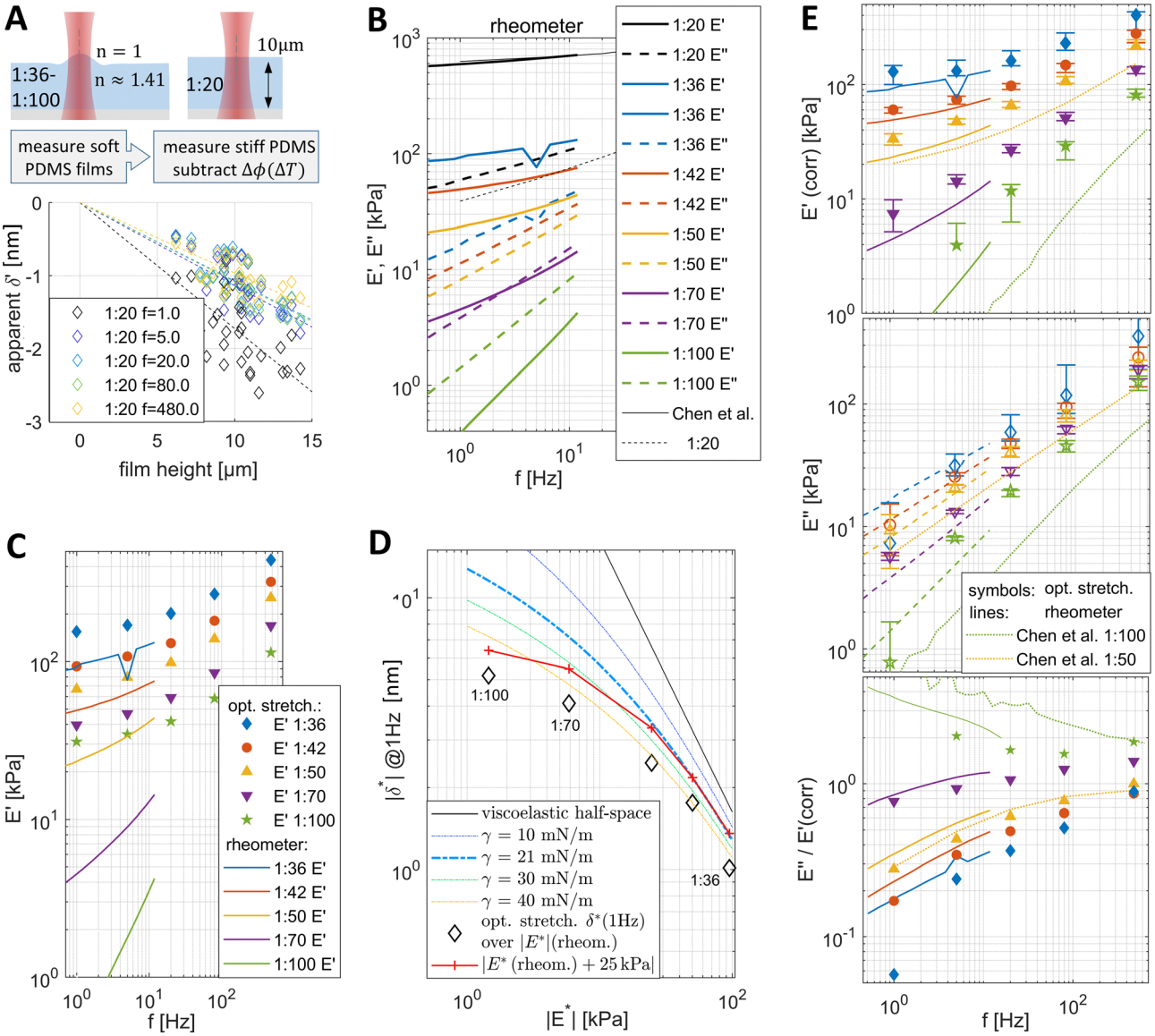

Fig. 4 Complex elastic modulus of 10 µm PDMS thin films measured with optical stretching in comparison with reference measurements acquired with a shear rheometer on 3 mm thick samples. (A) Negative apparent deformation observed on stiff films, presumably due to heating, which we subtract from the signal of the soft samples. (B) Viscoelasticity of the different mixing ratios determined with a shear rheometer and $E^* = 3G^*$. The 1 : 20 measurements agree well with the ones by Chen *et al.*,[40] the lower loss modulus for 1 : 20 might be due to the slight compression necessary to prevent the stiff film from slipping under the shear plate. (C) Storage modulus measured by optical stretching after subtraction of the negative signal from 1 : 20 films. There is a strong discrepancy, while the loss modulus is accurately measured (E, middle diagram). (D) Deformation over stiffness $|E^*|$ for a viscoelastic half-space, for an elastic half-space with different values of surface tension based on the Green's function in eqn (11), and deformation from optical stretching at 1 Hz over rheometer stiffness. The red line is the deformation resulting from a system with E^* (rheometer) with an elastic element $E^* = 25$ kPa in parallel, which agrees with the surface tension of PDMS of $\gamma = 21$ N m^{-1} for the stiff films. (E) Final E^* and loss tangent by optical stretching. Symbols are medians, errorbars are 25/75 percentiles. The storage modulus is corrected for the surface tension contribution as described in the text. The ratio of optical stretching to rheometer storage modulus in the upper diagram at 1 Hz corresponds to the inverse relative deviation of the symbols from the red line in D.

After subtracting the non-stretching contribution we obtain accurate results for E'' (Fig. 4E, middle), but not for E' (Fig. 4C). As the mixing ratio decreases, the measured storage modulus plateaus, while the actual film stiffness keeps decreasing. Errors of the deformation measurement limiting the maximum deformation can be ruled out. The interferometric detection allows to detect phase shifts of multiple π, and $\delta = 10$ nm corresponds to $\Delta\Phi = 1.3 \times 10^{-2}$ π. We additionally confirmed linearity between F and δ^* for $F_{ptp} = 400$ mW and $F_{ptp} = 1.5$ W for a 1 : 70 film (not shown).

The deviation of the storage modulus of soft films can largely be explained by considering surface tension and the corresponding non-dissipative restoring force. A direct way to determine the surface energy of PDMS is measuring the adhesion energy upon bringing in contact two PDMS surfaces. Sanchez *et al.* measured it for mixing ratios from 1 : 10

(21 mJ m^{-2}) to 1 : 50 (19.8 mJ m^{-2}), essentially independent of mixing ratio,[38] while ref. 41 and 42 found 25 mJ m^{-2} and 20.5 mJ m^{-2}, respectively, for 1 : 10. We therefore assume γ = 21 N m^{-1} for our thin films to estimate the impact of surface tension on our measurements. We also attempted to perform static contact angle measurements to estimate the surface energy. However both water and ethylene glycol droplets showed spreading on the timescale of a few minutes. Results were in the range of 5 to 22 mJ m^{-2} and inconsistent, with no clear dependence on mixing ratio (not shown).

The Green's function, which describes the deformation of an elastic half-space with surface tension resulting from a point force of unit amplitude, is given by[43]

$$G(r,s) = \frac{1}{4\gamma}[H_0(r/s) - Y_0(r/s)]. \quad (11)$$

H_0 is the zero order Struve function, Y_0 the Bessel function of the second kind, and $s = 2(1-\nu^2)\gamma/E$ is a lateral length scale below which the deformation is dominated by surface tension. Convolution with the stress profile of the optical stretcher allows to predict the deformation from optical stretching, analogous to eqn (2). In Fig. 4D, the dash-dotted lines show deformation over elasticity of an elastic half-space with different values of γ. For soft films, surface tension is dominant and the deformation is drastically reduced compared to the linear case γ = 0.

To our knowledge, there is no such model for the viscoelastic case, so we use a rather phenomenological approach to correct our data. The restoring force from surface tension is non-dissipative, caused by an increase in surface energy. When plotting deformation at 1 Hz from optical stretching over film stiffness in Fig. 4C, we see that the deformation plateaus for the soft films. In a mechanic equivalent circuit, this is a characteristic of an additional spring in parallel to a viscoelastic element. For our model we therefore introduce an elastic element E_2 = 25 kPa (red line), which agrees with γ = 21 N m^{-1} for the stiff films. This simplification has the advantage that we can correct the complex modulus for all frequencies, since surface tension is non-dissipative and thus independent of frequency.

For the comparison with the theoretical elastic half-space/surface tension curves we use $|E^*|$ and $|\delta^*|$ from our measurements. The reason is that the relative contribution of surface tension depends on $s = 2(1-\nu^2)\gamma/E$ in the elastic case (eqn (11)). In a viscoelastic system, the combined elastic and viscous forces ($|E^*|$) determine the total deformation, and thus the relative viscoelastic contribution in a system with surface tension.

For the stiff films, where the model agrees well with surface tension and where E'' is small, stretching yields slightly lower values $|\delta^*| = 0.75\left|\delta^*_{E_2}\right|$ $\left(0.81\left|\delta^*_{E_2}\right|\right)$ for 1 : 36 (1 : 42) than predicted by the model incorporating E_2. One possible explanation is that there is a systematic error produced by the optical stretching method.

For the deformation and the uncorrected complex modulus from stretching we can thus write $\delta^* = A/E^*$ ($A = \sqrt{2/\pi}(1-\nu^2)F\Big/w_0$, eqn (7)). Then $\delta/(0.78) = A/(E^* + E_2)$ and $A/\delta^* = E^*/0.78 + E_2/0.78$. We define a corrected complex modulus

$$E^*_{\mathrm{corr}} = A/\delta^* - E_2/0.78 \quad (12)$$

This yields a corrected storage modulus of about 1/0.78 = 1.28× the rheometer measurements for 1 : 36 and 1 : 42 at 1 Hz. By subtracting $E_2/0.78$ = 25 kPa/0.78 from our measurements, we correct for the non-dissipative contribution from surface tension. This is almost the same as subtracting $E'(1:100)$ = 31 kPa, the measured plateau value of the storage modulus (see Fig. 4C), which is higher than the actual modulus by ×81. However, since our model perfectly predicts the deformation for surface tension γ = 21 kPa for the stiff films, it is not a purely phenomenological approach.

The final storage and loss modulus together with the rheometer results are shown in Fig. 4. The storage modulus is slightly overestimated while the loss modulus is accurately measured, which leads to a slight underestimation of the loss tangent. The relative deviation of the optical stretching results from rheometer stiffness is compiled in Table 5.

3.1 Discussion

We investigated whether the discrepancy of the storage modulus might result from thin film properties that differ from bulk PDMS. Liu *et al.* claimed that there is stiffening for thin films[44] and speculated that it might result from alignment of the polymer chains during spin coating. We therefore prepared films by diluting the PDMS mixture in hexane at a weight ratio of 1 : 5, which allowed to produce 10 μm films at a spinning speed of 250 rpm instead of 7000 rpm. We find good agreement between both preparation methods (Fig. S8, ESI†), except for the 1 : 100 film, where we however measured only a single film with hexane. This seems to support the results from Li *et al.*[45] who carefully corrected AFM stiff substrate artifacts and found no thickness dependence down to a thickness of 1 μm.

We observe an overestimation of E' for the stiff films, while E'' is accurately measured. As the film stiffness decreases, the deviation for E' increases, which to a lesser degree also holds for E''. Furthermore, the deviation for E' decreases with increasing frequency. Surface tension can be expected to have the highest impact on the storage (not the loss) modulus, at low frequencies, and for soft films. We therefore believe that the discrepancy mainly stems from shortcomings of our model, which underestimates the contribution of surface tension.

Systematic errors in the optical stretching procedure might also contribute to the overestimation of E'. Potential errors

Table 5 Relative deviation of storage and loss modulus $E/E_{\mathrm{rheometer}}$ for the different mixing ratios, taken from Fig. 4 and averaged over 1 Hz and 5 Hz. $E'_{\mathrm{corr}}(1{:}100) \lesssim 0$ after subtraction of $E_2/0.78$ so no meaningful ratio can be given. The data point $E''(1:36)$ exhibits a large error bar and clearly deviates from the trend in Fig. 4 and was therefore excluded

PDMS mixing ratio	1 : 36	1 : 42	1 : 50	1 : 70	1 : 100
$E'_{\mathrm{corr}}/E'_{\mathrm{rheometer}}$	1.27	1.2	1.42	1.61	—
$E''/E''_{\mathrm{rheometer}}$	0.95	0.98	1.13	1.41	1.12

include a lensing effect, for which we estimated an upper bound of the error of 16% (Section S2.3, ESI†), or inaccuracies such as the estimation of the beam radius or an imperfect concentric positioning of stretching and detection laser spot. Such errors would decrease the measured δ^* by a constant factor, but not the phase angle, which contradicts the accurate measurement of E''. We can estimate an upper bound for this error of 1/0.78 = 1.28 – the deviation of E' for the stiff, elastic films, for which the model approximates a thin film with 21 mJ m^{-2} very well.

In conclusion, we showed that the optical stretcher is able to quantitatively measure the viscoelasticity of soft PDMS samples as long as surface tension is not dominant. The storage modulus deviates significantly for very soft films, however these have also not been successfully characterized with AFM. This confirms the assumptions concerning force application, height measurement and mechanical model.

4 Results from optical stretching of NIH-3T3 and HeLa cells

NIH-3T3 (n = 16) and HeLa cells (n = 18) were measured by optical stretching at multiple modulation frequencies. Fig. 5A shows the median storage and loss modulus for measurements above the nucleus and above the perinuclear cytoplasm as calculated by eqn (7). Most data points obey a weak power-law at lower frequencies with the storage and loss modulus changing at a constant ratio. This corresponds to a power-law compliance in time domain $J(t) = (1/E_0)(t/t_0)^{\beta}$, a feature that has been observed numerous times for adherent cells probed by different techniques.[46–48] The structural damping equation has been used to capture such behavior:[46,49]

$$E^* = E' + iE'' = E_0(\omega t_0)^{\beta}\Gamma(1-\beta)\cdot[\cos(\beta\pi/2) + i\sin(\beta\pi/2)] + i\omega\mu, \quad (13)$$

It adds an additional viscous term which accounts for an increase of the power-law exponent at higher frequencies. Such an increase of the exponent for high frequencies might indicate a transition to single filament response of the probed cytoskeletal network. An exponent of 0.75 is predicted for the single filament response of an entangled network of semiflexible polymers under macroscopic shear stress.[50]

Storage and loss moduli in Fig. 5 were simultaneously fitted with eqn (13). Most data points follow the fit, which also coincides with linear fits (on a double log scale) of storage and loss modulus individually, as indicated by the dashed lines. While NIH-3T3 cells exhibit a pure power-law behavior on the timescale from 1 s to 2 ms, HeLa cells show an increase of the loss modulus and a crossover around $\omega_{CO} \approx 0.5$ kHz. Some data points deviate from the fit, especially at low frequencies. Potential sources of errors include the rather low number of cells measured as well as the small deformation in

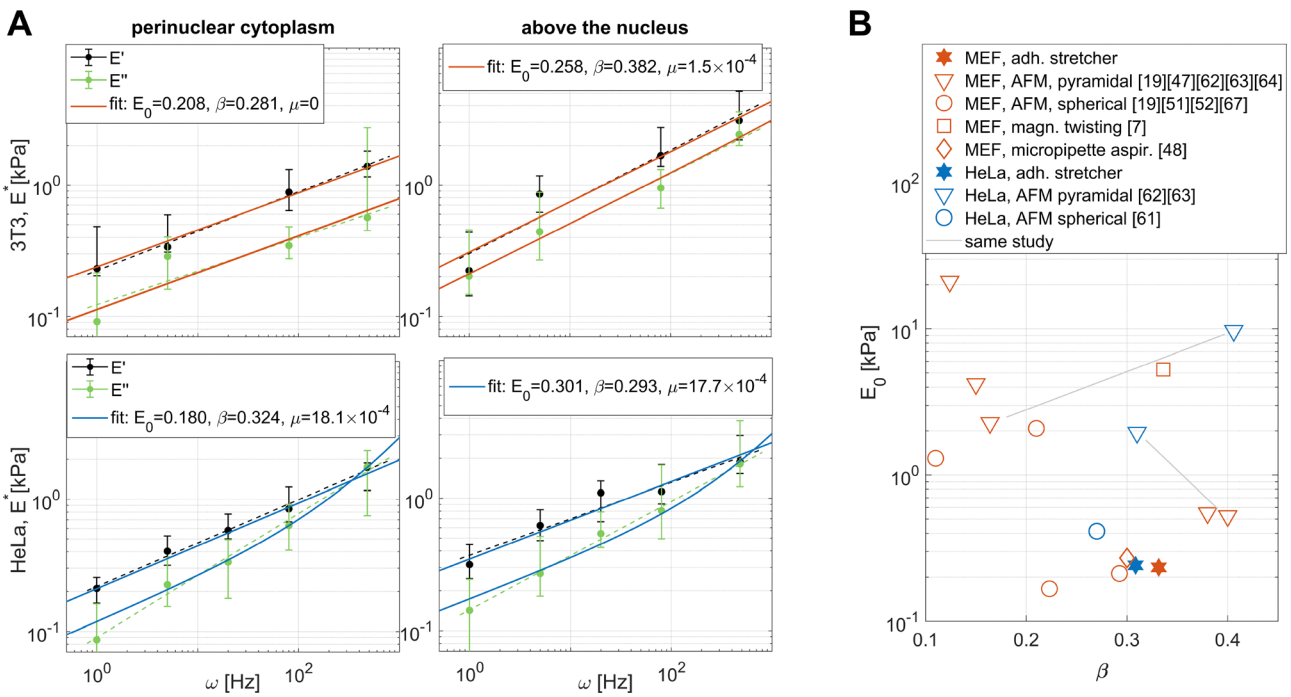

Fig. 5 (A) Median storage and loss modulus of adherent NIH-3T3 cells (n = 16) and HeLa cells (n = 18) at two different intracellular positions obtained by optical stretching.[12] Power-law parameters are extracted from simultaneous fit of storage and loss modulus with the structural damping equation (eqn (13)), while dashed lines indicate separate linear fits. The stretching laser was modulated at frequency ω and $P_{mean,sample} \approx 63$ mW; error bars extend from 25th to 75th percentile. (B) Comparison of the power-law parameters from A with results obtained by different techniques in literature. The orange symbols include mouse embryonic fibroblast cell lines that are not NIH-3T3. These publications are listed in Tables 6 and 7. Results above nucleus and perinuclear cytoplasm were averaged for optical stretching, and for literature data if both were available. Units of E_0 and μ are kPa and Pa s.

combination with the limited framerate and thus filter bandwidth. Some additional measurements (not shown) indicate, that the signal-to-noise ratio can be improved by choosing a higher laser power.

The same cells as in Fig. 5 were also measured in the cell periphery. The deformation is smaller, *i.e.* the cells appear stiffer (3T3: E_0 = 0.605 kPa, β = 0.285, μ = 0 Pa s; HeLa: 0.728 kPa, β = 0.257 kPa, $\mu = 3.5 \times 10^{-4}$ Pa s, Fig. S5, ESI†). The results are not included in the following comparison since most groups measure in the cell center and the signal-to-noise ratio for the periphery is lower.

Numerous authors have found that stiffness E_0 and fluidity β are correlated, *e.g.* between different cells of a sample[47,51,52] and for treatment with drugs affecting the stiffness.[46,53] We checked whether we also find this common feature of adherent cells by additionally fitting $E^*(\omega)$ of each cell and intracellular location (see Fig. S4, ESI†). When averaging nucleus and cytoplasm, our data reveal only a weak correlation (R^2 = 0.15), which is somewhat more pronounced when we include the periphery (R^2 = 0.41). We observe some noise on the individual cell level. The slope β is especially susceptible to noise at single 1 Hz or 480 Hz frequencies, which might conceal a steep $\ln E_0$–β correlation. This is why we continue our analysis with the median values.

4.1 Discussion

In Fig. 5B, the results obtained above the nucleus and the cytoplasm are averaged and compared to the power-law parameters obtained for these cell types in literature. For both cell types, E_0 is on the lower end of the range of literature results spanning two orders of magnitude, and β is in the center of the distribution that extends from $\sim$0.1–0.4.

Optical stretching gave similar results for NIH-3T3 and HeLa cells. A Wilcoxon's rank sum test based on E_0 and β for individual cells in Fig. S4 (ESI†) confirmed this: p = 0.40 (E_0) and p = 0.86 (β). Two AFM publications performing AFM indentation (connected by grey lines) compared the two cell types and found E_0 higher for HeLa cells, while the results for β were contradictive. Two more publications measured the Young's modulus of HeLa and 3T3 cells with AFM without a power-law description.[54,55] Contrary to the abovementioned results, they obtained a higher Young's modulus for 3T3 cells on a timescale of a few seconds – a quantity comparable to E_0 ($E_0 \approx |E(1\text{ Hz})|$. Literature does therefore not give an unambiguous answer on which cell line is stiffer.

The optical stretcher by Morisaku *et al.* found 3T3 cells stiffer than HeLa cells, with deformation over frequency showing a plateau below 1 kHz[11] – a purely elastic response. This setup did however not subtract non stretching contributions, whose magnitude is at 800 nm similar to stretching (see Fig. 3). Since it does not measure in a phase sensitive way it is not able to detect potential negative apparent deformations, that hint at other contributions.

log-normal distributed data with standard deviations of $\times$1.6 to $\times$4 were found for different techniques in cell rheology,[56] while $\times$2.05 was observed for the parameter E_0 in AFM indentation.[51] 2$\times$ means that 68.3% of the values are within the range 0.5$\times$ and 2$\times$ around the mean. The errorbars in Fig. 5, which represent 50% of the data points, do mostly not extend this far, so the spread seems reasonable. We additionally calculated the standard deviation of the logarithmized norm of δ^* for the cells analyzed here. For HeLa cells, a scatter plot of δ^* can be seen in in Fig. 3. For the calculation we set negative values to zero and removed one 480 Hz data point, where both δ' and δ'' were negative. The standard deviation, averaged over the 5 frequencies, is 1.82$\times$ for HeLa cells, and 2.02$\times$ for the 3T3 cells, which is within the expected range. A factor contributing to the variability from stretching is that two signals add up: the one from cellular mechanics and the one from non-stretching contributions. The latter signal is removed by subtracting the index-matched median, but the noise from cell-to-cell variability still remains.

Optical stretching applies the force to a rather large area of $A = \pi {w_0}^2 \approx 8.1\ \mu\text{m}^2$ and yields rather low E_0. It has been noticed before that AFM indentation with sharp pyramidal tips evaluated with a (visco-) elastic continuum model results in higher apparent Young's moduli than spherical tips.[53,57–59] This can also be observed in Fig. 5B and hints on possible explanations for the large discrepancy for E_0 between different publications. The impact of the width of the stress distribution on the elastic moduli obtained in different publications is elucidated in the next section. Rescaling these AFM studies to larger contact radii makes the results from optical stretching fit even better into the picture.

5 Meta-analysis of literature AFM results for E_0 and β and comparison to optical stretching

Publications where the stiffness of NIH-3T3 cells and HeLa cells was determined, and where the cells were modeled as a bulk material with a power-law compliance, are listed in Tables 6 and 7. For the sake of comparability, experiments using intracellular tracer particles were excluded, and the remaining ones are essentially the AFM data points in Fig. 5B.

AFM applies a force mainly perpendicularly to the cell surface, which is also the case for optical stretching. Magnetic twisting of a bead attached to the membrane applies a shear force, relies on estimates of the contact area, and is attached to the cytoskeleton *via* a focal adhesion.[7] Micropipette aspiration probes the whole cell,[48] Schierbaum *et al.* probed cells on soft substrates.[52] The latter three results were thus excluded from the following analysis.

In a linear elastic system, the width of the stress distribution also determines its depth, *i.e.* what material volume is probed. For the AFM studies, we estimate the contact radius a under the assumption of an elastic half-space, to obtain a measure for the width of the stress distribution. For optical stretching, it is given by w_0. These aspects are discussed in more detail in Section 2.3.

5.1 Correlation with contact radius

When plotting E_0 over the contact radius in Fig. 6A, a strong correlation becomes apparent, which holds for both cell types

Table 6 Publications with time-domain measurements of adherent NIH-3T3 cells, other mouse embryonic fibroblast cell lines (MEF), or HeLa cells, that were evaluated with a power-law and a bulk modulus. For this table, E_0 and β were computed to comply with eqn (13) with t_0 = 1 s, assuming incompressibility (E_0 = 3G_0). β: power-law coefficient; FDC: force–distance curve; (c): above the cytoplasm, (n): above the nucleus; ▽: pyramidal cantilever tip, (∅): spherical tip with diameter; δ: maximum deformation; F: maximum force. In some publications, the power-law was only valid at lower frequencies (*e.g.* ω < 100 Hz). Data from Ren *et al.* (Fig. 13) were digitized (software: ref. 60). δ, ∅ and F by Guan *et al.*[61] were estimated based on the text and their results for MDCKII cells (similar parameters and stiffness). All publications except for Ren *et al.*[62] used viscoelastic continuum models. Only the measurements by Sanchez/Garcia and Hecht/Schierbaum were conducted by the same lab

	β	E_0 [kPa]	Technique
NIH-3T3			
Sanchez *et al.* (2021)[63]	0.38 (n)/0.42 (c)	0.57 (n)/0.48 (c)	AFM FDC, ▽-tip, $F \approx 3$ nN, $\delta \approx 2$ μm, 37 °C
Garcia *et al.* (2020)[64]	0.38 (n) (ω < 20 Hz)	0.55 (n)	AFM FDC (speed varied), ▽-tip, F = 3 nN, $\delta \approx 1.5$ μm, 37 °C
Non-3T3 MEF			
Hecht *et al.* (2015)[47]	0.124	21	AFM creep experiment, ▽-tip $\delta \approx 0.15$ μm, F = 0.4 nN, (n) ≈ (c), 37 °C
Schierbaum *et al.* (2019)[52]	0.11	1.3	AFM creep experiment, ∅ = 2 μm, $\delta \approx 0.17$ μm, F = 1 nN, 37 °C
Ren *et al.* (2013)[62]	0.164 (n)	2.27 (n)	AFM FDC (speed varied), ▽ tip, δ, F, T not given; elastic Hertz model
HeLa			
Sanchez *et al.* (2021)[63]	0.29 (n)/0.33 (c)	2.35 (n)/1.54 (c)	AFM FDC, ▽-tip, $\delta \approx 1.3$ μm, $F \approx 3$ nN, 37 °C
Ren *et al.* (2013)[62]	0.41 (n)	9.7 (n)	AFM FDC (speed varied), ▽ tip, $\delta \approx 0.4$ μm, $F \approx 0.5$ nN elastic Hertz model, T not given
Guan *et al.* (2021)[61]	0.27 (n) (ω < 100 Hz)	0.41 (n)	AFM force relaxation, ∅ ∼ 16 μm tip, $\delta \sim 0.7$ μm, $F \sim 7$ nN, 37 °C
Weber *et al.* (2022)[65]	0.21 (n) (ω < 10 Hz)	t_0 not given	AFM force relaxation, ∅ 10 μm tip, δ = 1 μm, F = 1 nN, 37 °C

and pyramidal as well as spherical tips. Fitting the AFM data and rescaling E_0 to a contact radius equal to the $1/e^2$ beam radius w_0 of the optical stretcher results in good agreement between optical stretching and AFM indentation (Fig. 6B). w_0 is chosen, because for a given force, the deformation δ of an elastic half-space caused by a Gaussian beam with beam waist w_0 is only 6% larger than from spherical indentation with the contact radius $a = w_0$ (eqn (3) and (4)).

We find an equally strong correlation for E_0 over the projected contact area with the exponent as a free parameter (R^2 = 0.87 for $E_0 \propto A^{-0.54}$). Correlations with indentation depth are weaker: R^2 = 0.68 for $E_0 \propto \delta^{-1.57}$ with the exponent as a free parameter, and R^2 = 0.59 for $E_0 \propto \delta^{-1}$. Furthermore, for E_0 over δ, optical stretching strongly deviates from AFM since δ is two orders of magnitude lower than for AFM studies yielding similar E_0. These results indicate that the width of the stress distribution is more relevant than indentation depth or upward deformation.

Since E_0 and β vary by two orders of magnitude when probed by AFM, the model of a viscoelastic half-space with these material constants is apparently insufficient to describe adherent cells. Most of the difference scales with contact radius, so we now examine stress stiffening as a potential explanation.

5.2 Stress stiffening

On adherent cells, a linear relationship between stiffness and external shear stress applied by magnetic twisting cytometry[7,68] and by uniaxial stretching of whole adherent cells[69,70] has been found. Koenderink *et al.* showed, that reconstituted networks of actin and myosin in the presence of ATP also exhibit a linear relationship between stiffness and an external constant shear stress.[71] One can therefore write:

$$E_0 = E_{00} + a\sigma_e. \quad (14)$$

σ_e is an external stress, a is a factor of proportionality and E_{00} is a residual stiffness at zero external stress. In addition, several publications have shown that stiffness is proportional to the cellular prestress produced by the contractile actomyosin cytoskeleton,[52,72,73] which implies an equivalency of internal and external stress.

Fig. 6C shows E_0 over the external stress $\sigma_e = F/A_{projected}$ applied by the probe tip. To quantify the area of force application for AFM, we use the projected area πa^2 with the contact radius a to allow a better estimation of the maximum applied stress. Eqn (14) was fitted to the AFM data, with both sides logarithmized to achieve meaningful weighting. A linear relationship between external stress and stiffness describes most data points well. The data points from AFM with spherical tips and the lowest applied stresses indicate the formation of a plateau at $E_{00} \sim 0.27$ kPa. This value does not change when fitting only 3T3 cells. The results from optical stretching fit very well into that picture. The technique is capable of measuring the stiffness at stresses around 1 Pa (Table 2), several orders of magnitude lower than AFM indentation, while oscillatory measurements require an offset indentation.

We previously mentioned a commonly found correlation between stiffness E_0 and fluidity β, *e.g.* for different cells of a sample[47,51,52] and for treatment with drugs affecting the stiffness.[46,53] This correlation is thought to stem from varying cellular prestress, since it has been shown that both prestress and external stress change the power-law parameters in a correlated way,[7,52] also in reconstituted networks.[71]

Such a correlation is also present for the results from different publications performing AFM indentation on MEF

Table 7 Continuation of Table 6 for frequency domain measurements, most of them oscillatory AFM measurements of ~10 nm amplitude around an offset indentation δ. The cells were adherent to glass/PS except for the study by Zhou *et al.*, who used rounded cells. MTC: magnetic twisting cytometry, integrin-attached beads. Data from Rother (Fig. S4, ESI) and Kollmannsberger (Fig. 2 and 3) and were digitized (software: ref. 60); the crossover frequency ω_{CO} (where $E' = E''$), was calculated from the given power-law parameters. For Cai *et al.* and Hiratsuka *et al.*, δ was not given and was assumed the same as in ref. 66 (same author/method/cell line, same F and tip diameter). Rigato *et al.* was able to access frequencies up to 100 kHz and introduced a second power-law for this range, while for lower maximum frequencies, the structural damping equation (eqn (13)) was sufficient.[49,51,67] Only the publications by Cai/Hiratsuka were conducted by the same lab

	β	E_0 [kPa]	ω_{CO} [kHz]	Technique
NIH-3T3				
Rigato *et al.* (2017)[19]	0.21 (c) ($\omega < 1$ kHz)	2.08 (c)	53 (c)	AFM, ∅ 1 μm tip, δ = 0.3 μm, $F \approx$ 0.5 nN, T = RT
Rother *et al.* (2014)[49]	0.15	4.2	0.095	AFM, ▽-tip, δ = 0.55 μm, $F \approx$ 0.4 nN, 37 °C
Cai *et al.* (2013)[51]	0.31 (n)/0.28 (c)	0.23 (n)/0.20 (c)	0.35 (n)	AFM, ∅ 4.5 μm tip, $\delta \approx$ 1.5 μm, F = 0.65 nN, T unknown
Hiratsuka (2009)[67]	0.22 (n)	0.17 (n)	0.25 (n)	AFM, ∅ 4 μm tip, $\delta \sim$ 1.5 μm, F = 0.65 nN, T unknown
Zhou *et al.* (2010)[48]	0.3	0.27	$\gg$1 kHz	Micropipette aspiration of whole rounded cells, T = 30 °C
Non-3T3 MEF				
Kollmannsberger *et al.* 2011[7]	0.336	5.28	—	MTC, ∅ 4.5 μm beads, 37 °C
Optical stretching				
Optical stretching				

cells (Fig. 6D). It might however not hold for extreme cases, as two data points with exceptionally deep indentation with pyramidal tips (θ = 18°, $\delta \geq$ 1.5 μm, conducted by the same lab[63,64]) deviate from this trend and were excluded from the fit. The slope $\ln(E_0)/\beta$ = 26.65 is within the range of 26–28.3 found within samples of MEFs[47,52] and in a study with different cell types including MEFs, and drug treatments.[7] Ref. 52 shows, and ref. 7 claims, that intracellular prestress changes E_0 and β in this correlated manner. Our analysis indicates, that the same mechanism of stress stiffening, however by an external probe, might be responsible for the quantitative disagreement between stiffness values obtained in different publications.

It has been found already in 2001,[46] that for such a correlation of E_0 and β, a common $t_0 = \tau_0$ and $E_0 = 1/j_0$ in the structural damping equation (eqn (13), ignoring the high frequency viscous term) can be found so that E^* only depends on β. This is equivalent to

$$\ln(E_0) = \ln(1/j_0) - \beta \ln(t_0/\tau_0) \quad (15)$$

Based on the fitparameters in Fig. 6D, $j_0 = 3.6 \times 10^{-6}$ Pa^{-1} and $\tau_0 = 2.7 \times 10^{-12}$ s^{-1}. Inserting eqn (14) into eqn (15) yields:[7]

$$\beta = \frac{\ln j_0 (E_{00} + a\sigma_e)}{\ln \tau_0 / t_0}. \quad (16)$$

In Fig. 6E, eqn (16) is plotted with a dashed line, the MEF data points, except for the previously excluded ones follow.

The fluidity β of HeLa cells does not fit into the picture. There are some differences in the cytoskeletal organisation of HeLa and 3T3 cells. HeLa cells, for example, don't exhibit fibroblast-like stress fibers.[74] An argument against this idea is however that the negative correlation between E_0 and β is a phenomenon observed for many different cell lines and drug treatments.[46,47,51–53] The data from optical stretching (Fig. 5) were additionally evaluated for individual cells and intracellular locations. HeLa cells turned out to exhibit a negative correlation between E_0 and β as expected. It therefore seems more likely that there are other relevant experimental aspects that are not considered in this analysis.

5.3 Alternative interpretation: surface tension

The observed correlations hint on shortcomings of the viscoelastic half-space model. The absence of a stiff substrate effect was verified in two of the aforementioned publications.[47,63] The continuum assumption is supported by successful modeling of live cells as a thin layer.[75] In contrast, optical stretching at larger beam radii and different areas of the cell gave vastly inconsistent stiffness values when performing a stiff substrate correction,[12] questioning the continuum model.

The observation that pyramidal AFM tips tend to yield higher Young's moduli for adherent cells has been interpreted as a consequence of an effective surface tension. Ding *et al.*[76] conducted FEM simulations and obtained a correction term for the Hertz model that depends on the surface tension length scale $s = 2\gamma/E$ (with surface tension γ), and the contact radius a. Rewriting their result in a slightly different form with a modified contact radius $\tilde{a}$, it is:

$$E_a = E[1 + (s/\tilde{a})^\zeta]. \quad (17)$$

with the apparent Young's modulus E_a, obtained when treating the cell as an elastic half-space. For $s \ll \tilde{a}$, it approaches the Young's modulus E without surface tension, while for $s > \tilde{a}$, it is dominated by surface tension. The modified contact radius is similar to the contact radius a on an elastic half-space: $\tilde{a} = 1.149a \left(a = \sqrt{\delta R}\right)$, $1.06(\pi/2)a$ ($a = 2\tan\theta\delta/\pi$); ζ_{sphere} = 0.87 and $\zeta_{pyramid}$ = 0.92.

Fig. 7 reveals a correlation of E_0 with the modified contact radius $\tilde{a}$, similar to the contact radius in Fig. 6. The slope ζ = 0.895 has been chosen as the mean of spherical and pyramidal tips for simplicity. The fit yields $\gamma/\tilde{a} \gg E$, implying that all AFM data points were acquired in a surface tension dominated regime. For illustration purposes, the prediction of eqn (17) for s = 1 μm and

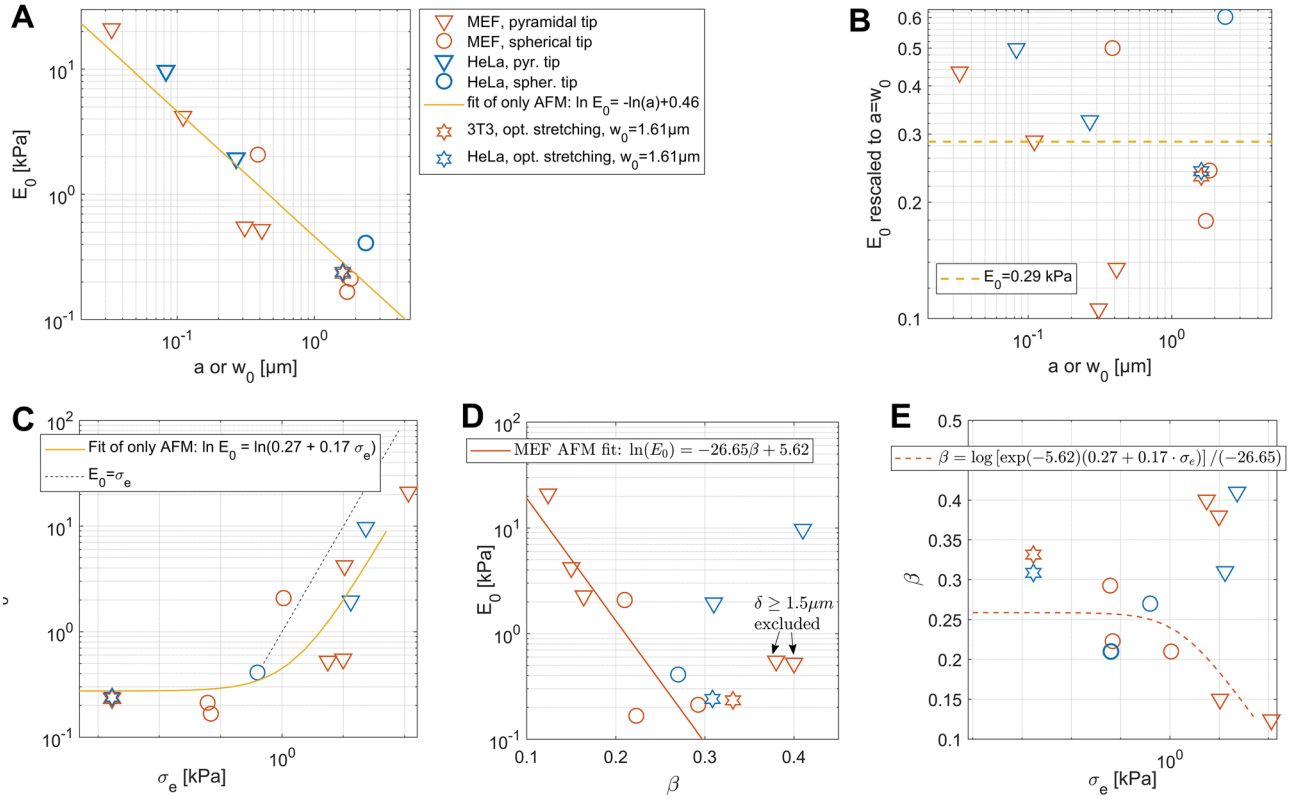

Fig. 6 (A) Correlations of the power-law parameters with contact radius a or $1/e^2$ beam radius w_0 across different publications that performed AFM indentation. Fit: R^2 = 0.87. Mainly two data points from the same lab with pyramidal tips and deep indentation >1.5 µm deviate (same as in D) (B) the fit from A is subtracted to rescale E_0 from the AFM results to a contact radius comparable to optical stretching. (C) The external stress applied by the probe tip is calculated as $\sigma_e = F/A_{projected}$, and only AFM data were fitted according to eqn (14). R^2 = 0.74. (D) Fit of AFM MEF data: R^2 = 0.78. Two AFM data points obtained by the same lab with pyramidal tips (θ = 18°) and very deep indentation $\delta \geq 1.5$ µm do not follow this trend and were excluded. (E) The dashed line is calculated from the fitparameters from (C) and (D). For all diagrams, AFM data were taken from Tables 6 and 7; ref. 52 was excluded due to soft substrates and ref. 62 since parameters for contact radius and stress were not given for 3T3 cells). The contact radius a for the AFM studies is estimated from the measurement parameters given in Tables 6 and 7 under the assumption of an elastic half-space. For a conical tip with half-angle θ, $a = (2/\pi)\delta \tan\theta$[18]), and for a spherical tip, $a = \sqrt{R\delta}$).

E = 0.25 kPa is indicated as a dashed line. There is no such transition to an elasticity dominated regime in the data.

Even though the slope is slightly too low, the hypothesis of all AFM measurements taking place in a surface tension dominated regime explains most of the variability in the AFM data (R^2 = 0.84). An argument against this hypothesis is, that β varies among these data points between 0.1 and 0.4. If the measurements were dominated by surface tension in the classical sense, changes in area would be stored as internal energy, and the response would be elastic. A more sophisticated model including viscoelasticity might resolve this issue. Such an approach was taken by Cordes *et al.*,[53] who fitted their indentation curves with a model assuming a viscoelastic shell with surface tension, and obtained more consistent results for AFM probe tips of different sizes and shapes.

5.4 Discussion and other potential explanations

In Fig. 6, we showed a strong correlation of the power-law parameters with the AFM contact radius between different studies. This is supported by the finding of many authors that the apparent stiffness is depth dependent[4,58,76–78] (but not ref. 65) and depends on the indenter size and shape.[4,53,57–59]

Phenomena that are known to distort AFM measurements include adhesion forces and an effect of a stiff underlying substrate. The latter can be excluded here since the publications with the highest stiffness use low indentation depths and sharp tips. Adhesion forces between cantilever tip and cell surface might on the other hand impact the apparent stiffness, if they were to significantly increase the contact area. Some of the publications in Tables 6 and 7 show force–distance-curves, and while they exhibit moderate negative adhesion forces upon retraction, no snapping into contact can be seen during the approach.[47,49,61] It can therefore be excluded that adhesion forces cause changes in apparent stiffness by two orders of magnitude.

High moduli for sharp tips have also been attributed to spatial inhomogeneities of biological samples.[79] The correlation with the contact radius observed here (Fig. 6) does however hold for contact radii from ~50 nm (smaller than the mesh size of the actin cortex) up to ~2 µm, and for pyramidal as well

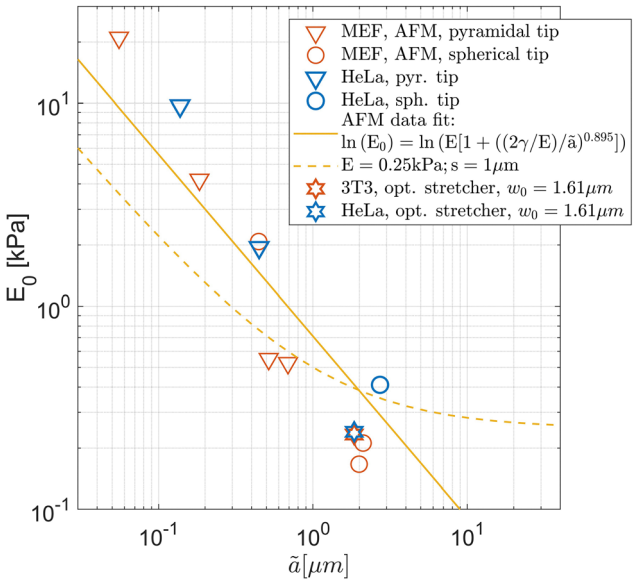

Fig. 7 E_0 over the modified contact radius from the same publications as in Fig. 6. The data points consist of all AFM studies referenced in Tables 6 and 7, except for ref. 52 and 65). $\tilde{a} = 1.149 w_0$ for optical stretching, as for a given force, deformation for stretching with a Gaussian beam and spherical indentation are approximately the same on an elastic half-space. Fit of the AFM data: $R^2 = 0.84$. The fitparameters exhibit large uncertainties, but $\gamma/\tilde{a} \gg E$, which is a surface tension dominated regime.

as spherical tips. While it thus appears unlikely that specific structures in combination with sharp tips are the main explanation, the lateral organisation of the cytoskeleton might play a role.

Some authors have shown, that more sophisticated models yield more consistent results for different indentation depths[76,78] and indenter sizes and shapes.[53,59] Most of these models feature a (visco-)elastic shell,[53,59] or surface tension.[53,76] These types of "surface models" handle pyramidal tips much better and appeal by their analogy to the actin cortex. In line with these findings, the surface tension model by Ding *et al.*[76] performs well in explaining the variation in E_0 in Fig. 7, while it cannot explain differences in fluidity.

Our alternative interpretation, the empirical model of a viscoelastic continuum with stress stiffening and fluidization (increase in β), can additionally explain the variation in β for 3T3 cells. On the other hand, the fact that optical stretching at larger beam radii with a stiff substrate correction gives inconsistent stiffness values questions the continuum model. In literature, stress stiffening has been observed for 3T3 cells with parallel plate rheology,[69] magnetic twisting cytometry[7] and substrate stretching and measurement of the deformability.[70] Their values for the plateau elasticity E_{00} at zero stress are however much higher: 1.68–10 kPa compared to 0.59 kPa in Fig. 6. Another inconsistency is, that Kollmannsberger *et al.*[7] found external and internal prestress additive, *i.e.* $E = e_0 + a(\sigma_p + \sigma_e)$. If this was the case for AFM indentation, very high external stresses due to small pyramidal tips (*e.g.* ref. 47) would dominate the response, and differences within the cell population due to different σ_p would not exist. Some of these studies however still show pronounced differences and E_0–β correlations, so σ_p and σ_e seem rather multiplicative.

Since the stress distribution induced by an AFM tip differs from *e.g.* shearing techniques, we checked whether stress stiffening has been examined for AFM indentation. Force–distance-curves were successfully fitted with an exponential stress stiffening model ($dF/d\delta \propto F$).[80] A model that simulates the cell as a 3D scaffold of elastic beams predicts nonlinearity for AFM indentation,[81] and a recently proposed four-parameter-model of cells is able to describe E_0–β correlations as well as stress stiffening.[82] In our perception, recent experimental studies on adherent cells however prefer the geometric models mentioned in the previous paragraph over stress stiffening to resolve issues like a depth dependence of the stiffness.

6 Discussion and conclusion

6.1 Technique

We presented a method of contact-free measurement of the viscoelasticity of adherent cells. A 800 nm-laser applies a very low tensile stress of $F_{max} \sim 1.7$ Pa while causing little heating of ~ 0.3 °C. The small deformations of <20 nm and the low RI difference yield a weak interferometric signal, which we extract by modulating the laser intensity with up to 0.5 kHz and lock-in filtering.

The signal from stretching at a given laser power scales with Δn^2, which allowed us to characterize much stiffer PDMS reference samples in air. We accurately measured the frequency dependent loss modulus of these thin films, and when considering surface tension we also get a good estimate of the storage modulus. This substantiates the adequacy of the technique for quantitative mechanical measurements.

We characterized 3T3 and HeLa cells by optical stretching and derived the power-law parameters E_0 and β. The latter agrees with values from literature, while E_0 agrees with publications that employed large probe tips and contact radii comparable to the beam radius from optical stretching.

Its contact-free nature avoids assumptions about tip-surface adhesion and the estimation of the contact area, and a calibration procedure in the classical sense is not needed. However, an inherent challenge of the interference-based detection method pose laser-induced changes in optical path length from effects other than membrane deformation. Intracellular effects such as thermophoresis cause negative phase shifts of a similar magnitude as the positive ones from stretching. In cells, we isolate, quantify and subtract this contribution by additionally measuring each sample in index-matched medium. Measuring two times at a known RI difference at the same time eliminates errors from incorrect assumptions on Δn. In PDMS thin films we find a similar unwanted negative signal. In the present configuration, we need to measure four times including reference measurements to characterize a cell, which makes it a rather low throughput method.

It can be substantially improved by using only a single NIR laser for stretching and detection. Splitting it into a stretching

and a reference beam with equal power would further induce the same amount of heating for both interfering beams and would render the reference measurements with the cell moved out of the beam path unnecessary. In our case however, the stretching laser, optimized for mode-coupled operation, turned out to produce an insufficiently stable interference pattern. An alternative is to make full use of the spatial resolution of the camera and perform quantitative phase imaging during stretching. This would take advantage of the probe-free nature of optical stretching and allow to observe the shape of the deformation. It is however challenging due to the different phase shifts produced by the stretching laser in and above the cell.

6.2 Biophysical insights

We performed a meta-analysis of publications that measured the aforementioned cell lines with AFM and analyzed their viscoelasticity with the same power-law model. Their results for E_0 span a range of about two orders of magnitude, but show a strong correlation with the contact radius and with force over contact area for both cell lines and AFM tip shapes. Optical stretching with the contact radius replaced by the beam radius fits well into the picture. The fact that similar stiffnesses are obtained at much lower deformation emphasizes the importance of the width of the stress distribution rather than the indentation depth.

We offer stress stiffening as a potential explanation of the correlations: E_0 is governed by the stress induced by the probe tip. This empirical model also explains the variability in β for 3T3/MEF cells, but not for HeLa cells. Optical stretching would then be in a strong position to measure cell mechanics unaltered by external stress.

In another interpretation, the disagreement is attributed to the inadequacy of the viscoelastic continuum assumption. In line with some rather recent works that apply more sophisticated models to resolve a dependence of the viscoelastic parameters on parameters such as tip shape,[53,76,78] we show that adding surface tension is able to explain most of the variability in E_0.

We hope that these insights contribute to improved study design and evaluation in the future.

Conflicts of interest

There are no conflicts to declare.

Data availability

Data and scripts for Fig. 2, 3 and 5 (accessible with Matlab v. 2024a) are available at Science Data Bank at **https://doi.org/10.57760/sciencedb.10165**.

Acknowledgements

The authors thank Iris Steiner, Nebal Altabl, Dorothee Erz and Carolin Grandy for cell culture and preparation of the samples, and Heinrich Hörber for fruitful discussions. A. Janik has received funding as a member of the graduate program GRK2203 from Deutsche Forschungsgesellschaft, which is gratefully acknowledged. We further thank the Institute for Functional Nanosystems, Ulm University, for providing the shear rheometer.

References

1 J. Guck, S. Schinkinger, B. Lincoln, F. Wottawah, S. Ebert, M. Romeyke, D. Lenz, H. Erickson, R. Ananthakrishnan, D. Mitchell, J. Käs, S. Ulvick and C. Bilby, *Biophys. J.*, 2005, **88**, 3689–3698.
2 S. Cross, Y.-S. Jin, J. Rao and J. Gimzewski, *Nat. Nanotechnol.*, 2007, **2**, 780–783.
3 M. Plodinec, M. Loparic, C. Monnier, E. Obermann, R. Zanetti-Dallenbach, P. Oertle, J. Hyotyla, U. Aebi, M. Bentires-Alj, R. Lim and C.-A. Schoenenberger, *Nat. Nanotechnol.*, 2012, **7**, 757–765.
4 P.-H. Wu, D.-B. Aroush, A. Asnacios, W.-C. Chen, M. Dokukin, B. Doss, P. Durand-Smet, A. Ekpenyong, J. Guck, N. V. Guz, P. Janmey, J. Lee, N. Moore, A. Ott, Y.-C. Poh, R. Ros, M. Sander, I. Sokolov, J. Staunton, N. Wang, G. Whyte and D. Wirtz, *Nat. Methods*, 2018, **15**, 491–498.
5 A. Nawaz, M. Urbanska, M. Herbig, M. Nötzel, M. Kräter, P. Rosendahl, C. Herold, N. Toepfner, M. Kubánková, R. Goswami, S. Abuhattum, F. Reichel, P. Müller, A. Taubenberger, S. Girardo, A. Jacobi and J. Guck, *Nat. Methods*, 2020, **17**, 595–599.
6 P. Kollmannsberger and B. Fabry, *Annu. Rev. Mater. Res.*, 2011, **41**, 75–97.
7 P. Kollmannsberger, C. T. Mierke and B. Fabry, *Soft Matter*, 2011, **7**, 3127–3132.
8 J. Guck, R. Ananthakrishnan, T. J. Moon, C. C. Cunningham and J. Käs, *Phys. Rev. Lett.*, 2000, **84**, 5451.
9 G. Choi, Z. Tang and W. Guan, *Nanotechnol. Precis. Eng.*, 2021, **4**, 045002.
10 T. Neckernuss, PhD thesis, Ulm University, 2018.
11 T. Morisaku and Y. Hiroharu, *Analyst*, 2018, **143**, 2397–2404.
12 A. Janik, PhD thesis, Ulm University, 2024.
13 A. V. Belashov, A. A. Zhikhoreva, T. N. Belyaeva, A. V. Salova, E. S. Kornilova, I. V. Semenova and O. S. Vasyutinskii, *Cells*, 2021, **10**, 2587.
14 Y. M. Efremov, T. Okajima and A. Raman, *Soft Matter*, 2020, **16**, 64–81.
15 J. Boussinesq, *Application des Potentiels a L'étude de L'Équilibre et du Mouvement des Solides Élastiques*, Gauthier-Villars, 1885.
16 K. L. Johnson, *Contact Mechanics*, Cambridge University Press, 1985.
17 H. Hertz, *J. Reine Angew. Math.*, 1882, **92**, 156–171.
18 V. L. Popov, M. Heß and E. Willert, *Handbook of Contact Mechanics*, Springer-Verlag GmbH, DE, 2019.
19 A. Rigato, A. Miyagi, S. Scheuring and F. Rico, *Nat. Phys.*, 2017, **13**, 771–775.

20 R. E. Mahaffy, C. K. Shih, F. C. MacKintosh and J. Käs, *Phys. Rev. Lett.*, 2000, **85**, 880–883.
21 P. D. Garcia and R. Garcia, *Biophys. J.*, 2018, **114**, 2923–2932.
22 D. Raucher and M. Sheetz, *Biophys. J.*, 1999, **77**, 1992–2002.
23 B. Pontes, N. Viana, L. Salgado, M. Farina, V. Neto and H. Nussenzveig, *Biophys. J.*, 2011, **101**, 43–52.
24 K. Schumacher, A. Popel, B. Anvari, A. Brownell and W. E. Spector, *Phys. Rev. E:Stat., Nonlinear, Soft Matter Phys.*, 2009, **80**, 041905.
25 K. Kim and J. Guck, *Biophys. J.*, 2020, **119**, 1946–1957.
26 T. Ford, J. Graham and D. Rickwood, *Anal. Biochem.*, 1994, **220**, 360–366.
27 Y. Yoshitake, S. Mitani, K. Sakai and K. Takagi, *J. Appl. Phys.*, 2005, **97**, 024901.
28 G. Abbate, U. Bernini, E. Ragozzino and F. Somma, *J. Phys. D: Appl. Phys.*, 1978, **11**, 1167.
29 C. Huster, D. Rekhade, A. Hausch, S. Ahmed, N. Hauck, J. Thiele, J. Guck, K. Kroy and G. Cojoc, *New J. Phys.*, 2020, **22**, 085003.
30 F. Català, F. Marsà, M. Montes-Usategui, A. Farré and E. Martín-Badosa, *Sci. Rep.*, 2017, **7**, 16052.
31 S. Kedenburg, M. Vieweg, T. Gissibl and H. Giessen, *Opt. Mater. Express*, 2012, **2**, 1588–1611.
32 M. Wolff, J. Mittag, T. Herling, E. De Genst, C. Dobson, T. Knowles, D. Braun and A. Buell, *Sci. Rep.*, 2016, **6**, 22829.
33 R. Piazza, *Soft Matter*, 2008, **4**, 1740–1744.
34 T. Mang, S. Lindemann and A. Gigout, *Int. J. Mol. Sci.*, 2020, **21**, 531.
35 P. C. Sontum, C. Christiansen, V. Kasparkova and T. Skotland, *Int. J. Pharm.*, 1998, **169**, 203–212.
36 S. Girardo, N. Träber, K. Wagner, G. Cojoc, C. Herold, R. Goswami, R. Schlüßler, S. Abuhattum, A. Taubenberger, F. Reichel, D. Mokbel, M. Herbig, M. Schürmann, P. Müller, T. Heida, A. Jacobi, E. Ulbricht, J. Thiele, C. Werner and J. Guck, *J. Mater. Chem. B*, 2018, **6**, 6245–6261.
37 E. K. Dimitriadis, F. Horkay, J. Maresca, B. Kachar and R. S. Chadwick, *Biophys. J.*, 2002, **82**, 2798–2810.
38 Y. Yu, D. Sanchez and N. Lu, *J. Mater. Res.*, 2015, **30**, 2702–2712.
39 Kenry, M. C. Leong, M. H. Nai, F. C. Cheong and C. T. Lim, *Procedia IUTAM*, 2015, **12**, 20–30.
40 L. Chen, E. Bonaccurso, P. Deng and H. Zhang, *Phys. Rev. E*, 2016, **94**, 063117.
41 M. Dirany, L. Dies, F. Restagno, L. Léger, C. Poulard and G. Miquelard-Garnier, *Colloids Surf., A*, 2015, **468**, 174–183.
42 M. K. Chaudhury, T. Weaver, C. Y. Hui and E. J. Kramer, *J. Appl. Phys.*, 1996, **80**, 30–37.
43 J. M. Long and G. F. Wang, *Mech. Mater.*, 2013, **56**, 65–70.
44 M. Liu, J. Sun, Y. Sun, C. Bock and Q. Chen, *J. Micromech. Microeng.*, 2009, **19**, 035028.
45 L. Li, N. Alsharif and K. A. Brown, *J. Phys. Chem. B*, 2018, **122**, 10767–10773.
46 B. Fabry, G. N. Maksym, J. P. Butler, M. Glogauer, D. Navajas and J. J. Fredberg, *Phys. Rev. Lett.*, 2001, **87**, 148102.
47 F. M. Hecht, J. Rheinlaender, N. Schierbaum, W. H. Goldmann, B. Fabry and T. E. Schäffer, *Soft Matter*, 2015, **11**, 4584–4591.
48 E. H. Zhou, S. T. Quek and C. T. Lim, *Biomech. Model. Mechanobiol.*, 2010, **9**, 563–572.
49 J. Rother, H. Nöding, I. Mey and A. Janshoff, *Open Biol.*, 2014, **4**, 140046.
50 F. Gittes and F. C. MacKintosh, *Phys. Rev. E: Stat. Phys., Plasmas, Fluids, Relat. Interdiscip. Top.*, 1998, **58**, R1241–R1244.
51 P. Cai, Y. Mizutani, M. Tsuchiya, J. M. Maloney, B. Fabry, K. J. Van Vliet and T. Okajima, *Biophys. J.*, 2013, **105**, 1093–1102.
52 N. Schierbaum, J. Rheinlaender and T. E. Schäffer, *Soft Matter*, 2019, **15**, 1721–1729.
53 A. Cordes, H. Witt, A. Gallemí-Pérez, B. Brückner, F. Grimm, M. Vache, T. Oswald, J. Bodenschatz, D. Flormann, F. Lautenschläger, M. Tarantola and A. Janshoff, *Phys. Rev. Lett.*, 2020, **125**, 068101.
54 K. Ren, J. Feng, H. Bi, Q. Sun, X. Li and D. Han, *Small*, 2023, **19**, 2303610.
55 W. Gu, X. Bai, K. Ren, X. Zhao, S. Xia, J. Zhang, Y. Qin, R. Lei, K. Chen, L. Chang, Y. Zeng, J. Li and G. Xing, *Nanoscale*, 2018, **10**, 1750–1758.
56 B. D. Hoffman, G. Massiera, K. V. Citters and J. Crocker, *Proc. Natl. Acad. Sci. U. S. A.*, 2006, **103**, 10259–10264.
57 J. Zemła, J. Bobrowska, A. Kubiak, T. Zieliński, J. Pabijan, K. Pogoda, P. Bobrowski and M. Lekka, *Eur. Biophys. J.*, 2020, **49**, 485–495.
58 N. Guz, M. Dokukin, V. Kalaparthi and I. Sokolov, *Biophys. J.*, 2014, **107**, 564–575.
59 R. Vargas-Pinto, H. Gong, A. Vahabikashi and M. Johnson, *Biophys. J.*, 2013, **105**, 300–309.
60 *PlotDigitizer: Version 3.1.5*, 2023, **https://plotdigitizer.com**.
61 D. Guan, Y. Shen, R. Zhang, P. Huang, P. Lai and P.-Y. Tong, *Phys. Rev. Res.*, 2021, **3**, 043166.
62 J. Ren, S. Yu, N. Gao and Q. Zou, *Phys. Rev. E: Stat., Nonlinear, Soft Matter Phys.*, 2013, **88**, 052711.
63 J. G. Sanchez, F. M. Espinosa, R. Miguez and R. Garcia, *Nanoscale*, 2021, **13**, 16339–16348.
64 P. D. Garcia, C. R. Guerrero and R. Garcia, *Nanoscale*, 2020, **12**, 9133–9143.
65 A. Weber, R. Benitez and J. L. Toca-Herrera, *Microsc. Res. Tech.*, 2022, **85**, 3284–3295.
66 P. Cai, R. Takahashi, K. Kuribayashi-Shigetomi, A. Subagyo, K. Sueoka, J. M. Maloney, K. J. Van Vliet and T. Okajima, *Biophys. J.*, 2017, **113**, 671–678.
67 S. Hiratsuka, Y. Mizutani, M. Tsuchiya, K. Kawahara, H. Tokumoto and T. Okajima, *Ultramicroscopy*, 2009, **109**, 937–941.
68 N. Wang, J. P. Butler and D. E. Ingber, *Science*, 1993, **260**, 1124–1127.
69 P. Fernández, P. Pullarkat and A. Ott, *Biophys. J.*, 2006, **90**, 3796–3805.
70 E. P. Canović, D. T. Seidl, S. R. Polio, A. A. Oberai, P. E. Barbone, D. Stamenović and M. L. Smith, *Biomech. Model. Mechanobiol.*, 2014, **13**, 665–678.
71 G. H. Koenderink, Z. Dogic, F. Nakamura, P. M. Bendix, F. C. MacKintosh, J. H. Hartwig, T. P. Stossel and D. A. Weitz, *Proc. Natl. Acad. Sci. U. S. A.*, 2009, **106**, 15192–15197.

72 N. Wang, I. Tolić-Nørrelykke, J. Chen, S. M. Mijailovich, J. P. Butler, J. J. Fredberg and D. Stamenović, *Am. J. Physiol. Cell Physiol.*, 2002, **282**, C606–C616.
73 C. Y. Park, D. Tambe, A. M. Alencar, X. Trepat, E. H. Zhou, E. Millet, J. P. Butler and J. J. Fredberg, *Am. J. Physiol.: Cell Physiol.*, 2010, **298**, C1245–C1252.
74 L. Roberts, H. Glenn, C. Hahn and B. Jacobson, *J. Cell. Physiol.*, 2003, 196–205.
75 N. Gavara and R. Chadwick, *Nat. Nanotechnol.*, 2012, **7**, 733–736.
76 Y. Ding, J. Wang, G.-K. Xu and G.-F. Wang, *Soft Matter*, 2018, **14**, 7534–7541.
77 K. Pogoda, J. Jaczewska, J. Wiltowska-Zuber, O. Klymenko, K. Zuber, M. Fornal and M. Lekka, *Eur. Biophys. J.*, 2012, **41**, 79–87.
78 S. Kontomaris, A. Georgakopoulos, A. Malamou and A. Stylianou, *Mech. Mater.*, 2021, **158**, 103846.
79 D. Sicard, L. Fredenburgh and D. Tschumperlin, *J. Mech. Behav. Biomed. Mater.*, 2017, **74**, 118–127.
80 K. Hayashi and M. Iwata, *J. Mech. Behav. Mater.*, 2015, **49**, 105–111.
81 N. Zolfaghari, M. Zand and R. Dargazany, *J. Appl. Comput. Mech.*, 2019, **50**, 289–294.
82 J.-T. Hang, Y. Kang, G.-K. Xu and H. Gao, *Nat. Commun.*, 2021, **12**, 6067.

